

1  
2 **Seismo-acoustic and GNSS monitoring of a record-breaking storm**  
3 **in the Black Sea: Evidence of climate change and intensifying**  
4 **natural hazards**

5  
6 Laura Petrescu<sup>1,2,\*</sup>, Bogdan Antonescu<sup>1,2</sup>, Sorin Nistor<sup>3</sup>, Iustin Floroiu<sup>4,5</sup>, Dragoş Ene<sup>1</sup>, Daniela  
7 Ghica<sup>1</sup>, Constantin Ionescu<sup>1</sup>, Andrei Anghel<sup>4</sup>, Mihai Datcu<sup>4</sup>

- 8  
9 1. National Institute for Earth Physics, Magurele, Romania  
10 2. University of Bucharest, Faculty of Physics, Magurele, Romania  
11 3. University of Oradea, Faculty of Construction, Cadaster and Architecture, Oradea,  
12 Romania  
13 4. Politehnica University of Bucharest, Faculty of Electronics, Telecommunications and  
14 Information Technology, Bucharest, Romania  
15 5. Politehnica University of Bucharest, Doctoral School of Electronics,  
16 Telecommunications & Information Technology, Bucharest, Romania

17  
18 \* [laura.petrescu@infp.ro](mailto:laura.petrescu@infp.ro)

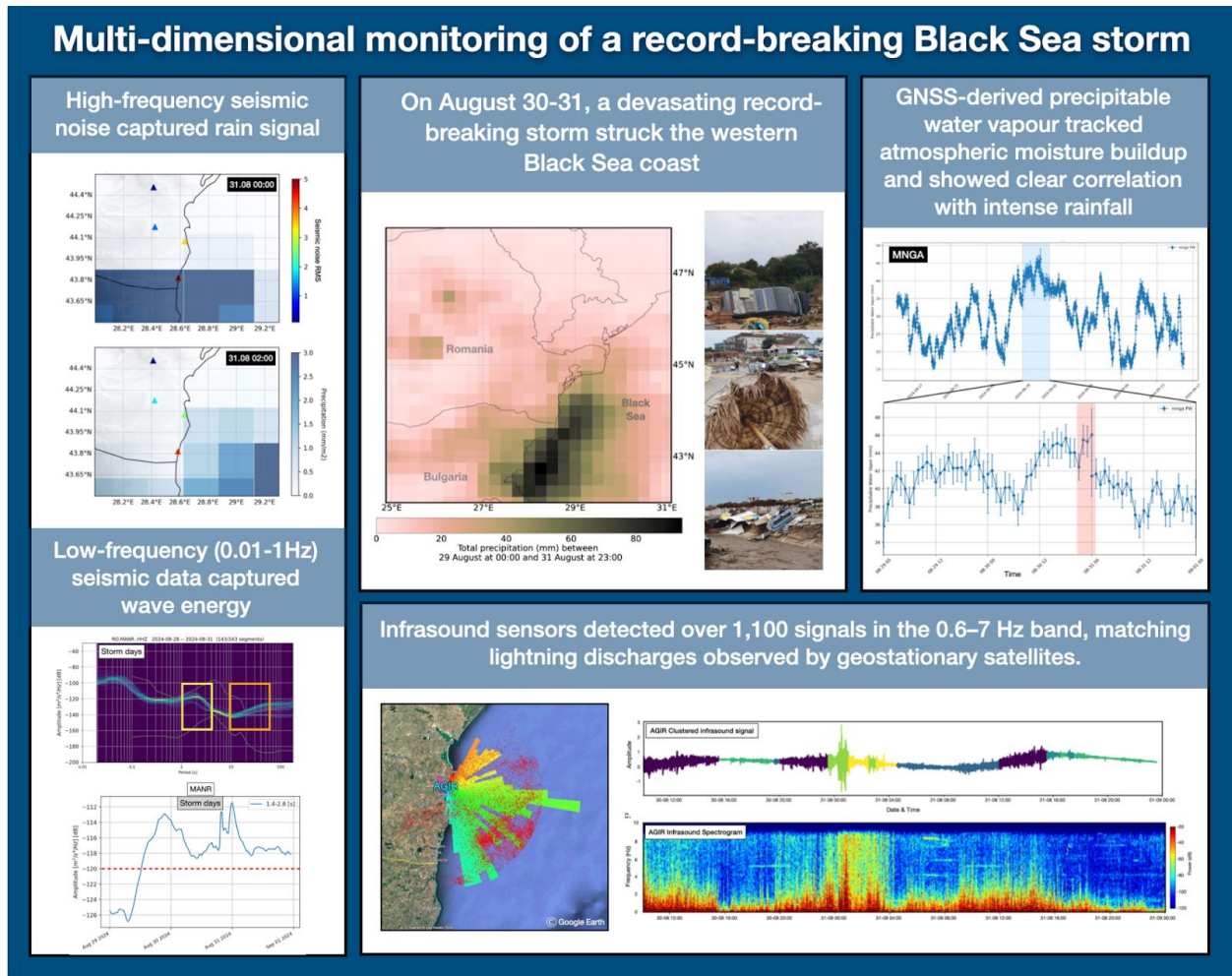
19  
20 **Abstract**  
21

22 In August 2024, a devastating storm struck Romania's Black Sea coast, setting new precipitation  
23 records and highlighting the increasing frequency of extreme weather events. This study explores  
24 the integration of non-conventional sensors (seismic, GNSS, infrasound, and satellite data) with  
25 ERA5 meteorological reanalysis to monitor storm dynamics. High-frequency (>30 Hz) seismic  
26 signals captured precipitation, while microseismic bands (0.1-1Hz) reflected wave-induced ground  
27 motion. Analysis of infrasound data via unsupervised learning delineated periods of acoustic  
28 quiescence from storm-related activity. The temporal evolution of these infrasound states  
29 coincided with distinct patterns in seismic ground motion, suggesting a shared origin in the storm's  
30 atmospheric dynamics. The infrasound array also detected over 1,100 signals in the 0.6-7 Hz band,  
31 matching lightning discharges observed by geostationary satellites. GNSS data recorded a buildup  
32 of precipitable water vapor that peaked concurrently with intense rainfall, following a multi-day  
33 increase that preceded the main storm phase. This study highlights the value of integrating diverse,  
34 non-traditional datasets to enhance the resolution and depth of storm analysis. Their combined use  
35 offers a more holistic understanding of storm evolution and supports the development of improved  
36 early-warning systems in vulnerable coastal regions.

37

38 **Graphical abstract**

39



40

41

42

43

44

45

46

47

## 48 **1. Introduction**

49 Climate change has become a critical global issue, with far-reaching effects on weather patterns  
50 and the frequency and intensity of extreme events (Stott, 2016). These changes are not only  
51 contributing to more severe weather events but also altering the timing, location, and duration of  
52 storms, making them harder to predict and manage (Bengtsson et al., 2006). Understanding how  
53 to effectively monitor and predict the behavior of storms, particularly extreme ones, is crucial for  
54 improving forecasting models, enhancing early warning systems, and mitigating their impacts on  
55 both natural and human systems.

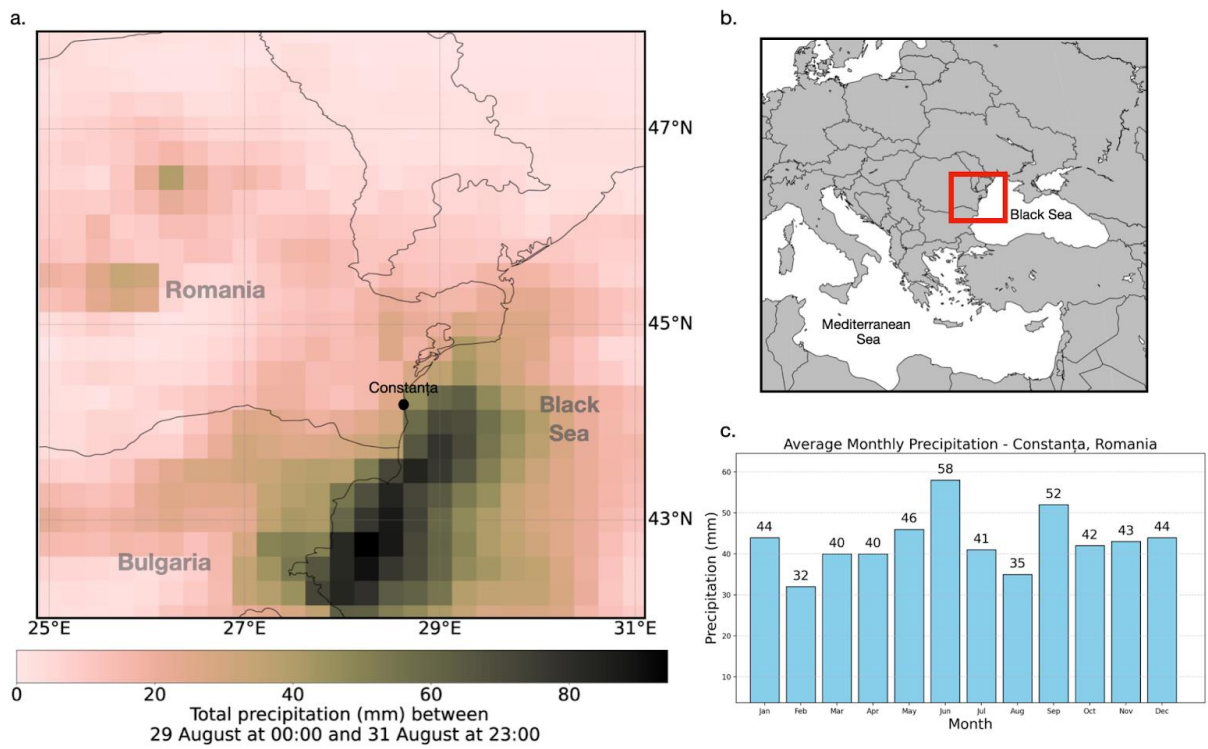
56 Traditional meteorological monitoring relies heavily on ground-based stations, weather radars, and  
57 satellite observations to track and predict storm behavior (Kober and Tafferner, 2009). These  
58 systems have been the backbone of weather forecasting for decades, providing valuable data on  
59 temperature, pressure, wind speed, and precipitation. However, while these methods are effective,  
60 they often have limitations in terms of spatial coverage (e.g. Sokol et al., 2021), particularly in  
61 remote or hard-to-reach areas. Additionally, they may struggle to capture certain atmospheric  
62 phenomena in real-time. As a result, non-conventional monitoring methods are increasingly being  
63 integrated into storm tracking efforts to complement existing meteorological approaches (e.g. Bosy  
64 et al., 2012; Burtin et al., 2016; Diaz et al., 2023; Coviello et al., 2024) .

65 In this context, our study focuses on the integration of alternative environmental datasets, including  
66 GNSS stations, infrasound sensors, and seismic data, to track the dynamics of an extreme storm  
67 event, as part of a national climate change resilience strategy, implemented through the DTE  
68 Climate project (<https://dteclimate.upb.ro/>). GNSS data provide valuable information on  
69 atmospheric water vapor, helping to track moisture changes that influence storm formation and  
70 intensity (Bosy et al, 2012; Marut et al., 2022). Infrasound sensors detect low-frequency acoustic  
71 waves generated by storm activity, such as lightning or large-scale weather system movements  
72 like microbaroms (e.g. Landès et al., 2012). Seismic data, though traditionally used for earthquake  
73 monitoring, can also record vibrations caused by storm-induced pressure changes, making it useful  
74 for detecting rainstorms, floods, or tropical cyclones (e.g. Retailleau and Gualtieri, 2021). Through  
75 the integration of these diverse sensor networks, our work highlights their synergy in improving  
76 storm detection, monitoring capabilities, and early warning systems, contributing to more robust  
77 climate resilience strategies.

## 78 **2. Study area and storm overview**

79  
80 The Black Sea region (Figure 1) is characterized by a unique combination of geographic and  
81 meteorological features that significantly influence its climate and weather patterns. Nestled  
82 between Europe and Asia, the Black Sea is bordered by six countries with diverse landscapes, from  
83 mountainous areas to flat plains. This geography, combined with the Black Sea's relatively shallow  
84 waters compared to oceanic environments and its connection to the Mediterranean through the  
85 Bosphorus Strait, creates an environment where rapid changes in weather are common.  
86 Understanding the dynamics of these extreme weather events is crucial, as they can have a  
87 profound impact on the environment, economy, and daily life in the region. Monitoring such events  
88 is key to improving our ability to predict their occurrence and intensity. By studying the complex  
89 atmospheric processes that govern these storms, we can enhance predictive models and refine early

90 warning systems, ultimately helping to mitigate the risks and protect the communities and  
91 ecosystems most vulnerable to these extreme weather phenomena.



92  
93 *Figure 1. a. Total precipitation accumulated (in mm, shaded according to the scale) between 29*  
94 *August 00 UTC and 31 August 23:00 UTC extracted from ERA5 data. b. Map of Europe with red*  
95 *square marking the study region; c. Average monthly precipitation rates in Constanța, Romania.*

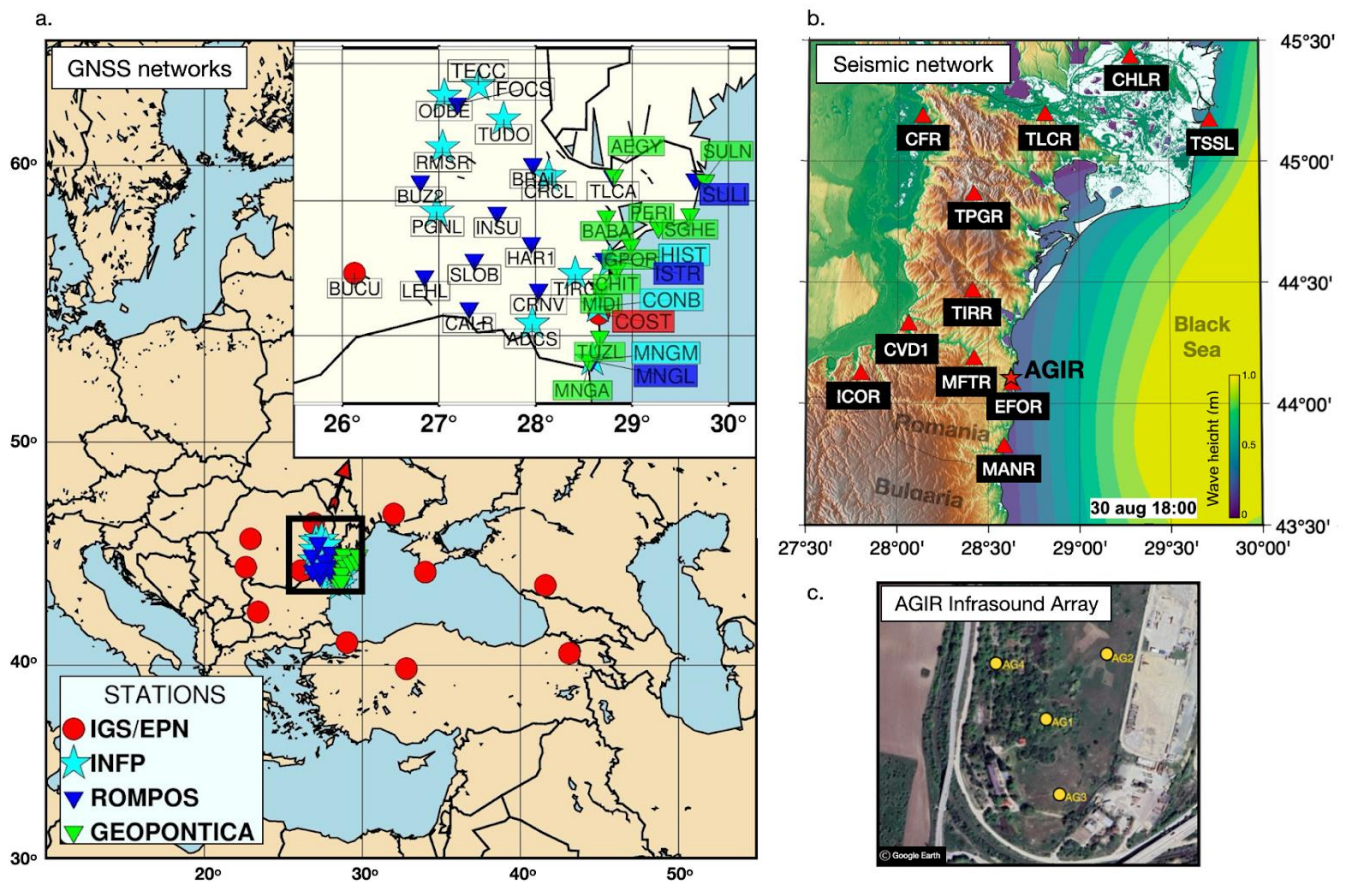
96 In August 2024, Romania experienced severe flooding, largely driven by a storm that brought  
97 unusual precipitation patterns to the Black Sea coastal region. Exceptional precipitation totals were  
98 recorded over south-eastern Romania in particular in Mangalia (234.7 mm), Agigea (145 mm),  
99 and Tuzla (118 mm), leading to significant flooding in coastal towns (Figure 1). Over 800  
100 emergency calls prompted large-scale intervention by ISU Dobrogea, focusing on evacuations,  
101 debris clearance, and infrastructure restoration (Antonescu et al. 2024). According to the National  
102 Meteorological Agency official records ([https://www.meteoromania.ro/clim/caracterizare-lunara/cc\\_2024\\_08.html](https://www.meteoromania.ro/clim/caracterizare-lunara/cc_2024_08.html)), one of the coastal stations at Mangalia, recorded a total of 343.6 mm of  
103 precipitation in August 2024, breaking the previous record of 159.1 mm from 1947, and  
104 significantly surpassing the average monthly precipitation values for this area (Figure 1c). A  
105 remarkable 234.7 mm of this total fell in a single day on August 31, 2024, highlighting the event's  
106 exceptional intensity.  
107

108 An analysis conducted by ClimaMeter ([www.climameter.org](http://www.climameter.org), Faranda et al. 2024, Antonescu et  
109 al. 2024) immediately after the event, showed that low pressure systems similar to the one that  
110 caused the floods typically result in reduced rainfall (7 mm day<sup>-1</sup>, or up to 15% less) in eastern  
111 Romania compared to historical trends. However, this particular storm led to a significant local  
112 increase in precipitation, particularly in Constanța, one of the coastal cities severely affected by

113 the flooding. In Constanța, daily rainfall reached up to  $5 \text{ mm day}^{-1}$ , or up to 10% more than usual,  
 114 marking a notable deviation from the region’s typical weather behavior. The changes in  
 115 precipitation that contributed to the flooding are largely attributed to human-induced climate  
 116 change, with natural climate variability likely playing a modest role. As climate change continues  
 117 to influence weather patterns, understanding the connection between changing precipitation levels  
 118 and extreme weather events like flooding is crucial for improving forecasting and resilience in the  
 119 face of such disasters.

### 120 3. Data and Methods

121 The analysis of the storm event integrates a variety of data sources and methodologies to provide  
 122 a comprehensive understanding of its dynamics. Seismic data, infrasound measurements, GNSS  
 123 water vapor data, and ERA5 reanalysis data are all utilized to capture different aspects of the  
 124 storm’s behavior (Figure 2). Seismic data offers insights into ground vibrations and atmospheric  
 125 disturbances, while infrasound monitoring detects low-frequency acoustic signals generated by  
 126 lightning and other meteorological phenomena. GNSS water vapor data provides valuable  
 127 information on atmospheric moisture. Additionally, ERA5 reanalysis data (Hersbach et al. 2020),  
 128 which provides detailed atmospheric and wave dynamics data, helps contextualize the storm’s  
 129 impact within broader weather patterns. Together, these diverse data sources enable a multifaceted  
 130 approach to studying the storm and its effects.



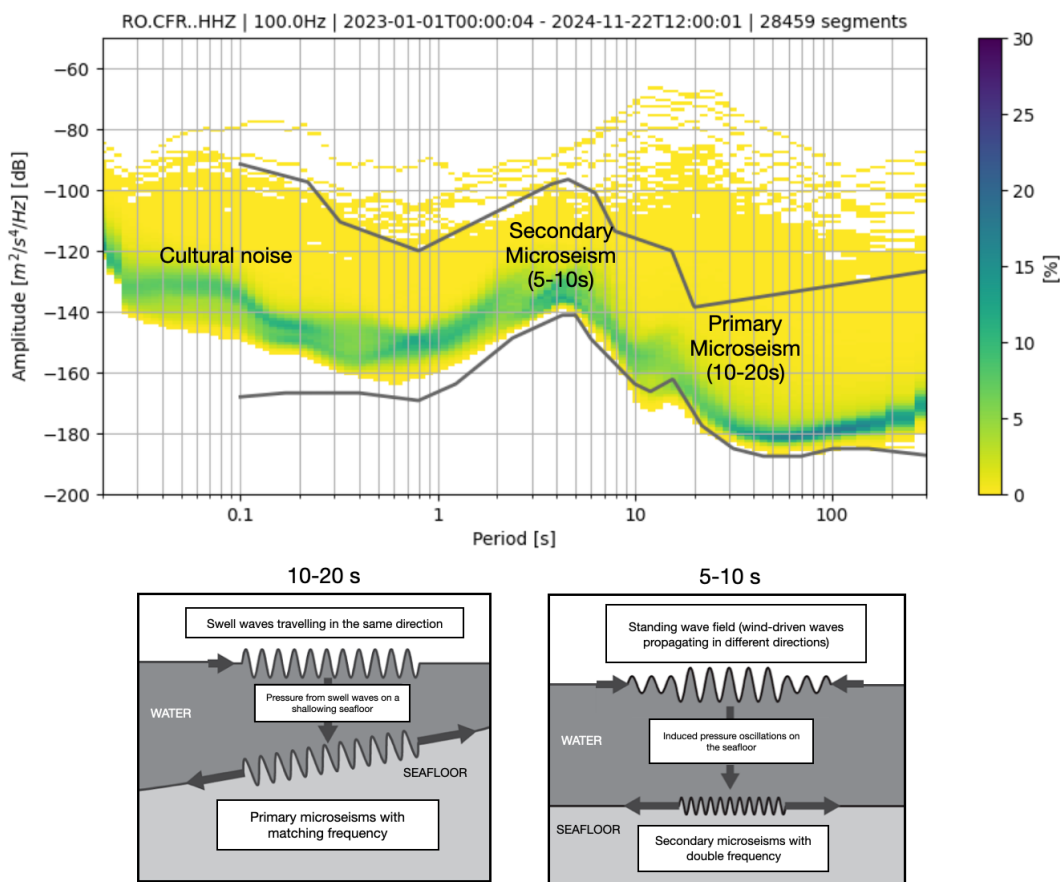
131

132 *Figure 2. a. Map of Europe and the Black Sea coast showing GNSS stations and their belonging networks*  
133 *used for analysis in this study. b. Map of the Romanian sea coast showing seismic stations (red triangles)*  
134 *and the location of the AGIR infrasound array (star). Coloured contours represent total wave height at*  
135 *18:00 on the 30th of August 2024 from ERA5 reanalysis data. c. The layout of the AGIR infrasound array.*

### 136 **3.1 Seismic Data**

137 Seismic data represents vibrations of the Earth's surface, commonly referred to as seismic noise.  
138 These low-amplitude movements are recorded across the Earth's surface and are traditionally used  
139 to study the Earth's internal structure and detect earthquakes. Recently, it has increasingly found  
140 applications in meteorology and hydrology, particularly for monitoring weather events (e.g. Dias  
141 et al. 2023; Hua et al., 2023), destructive flood episodes (Burtin et al., 2016), ocean storms, and  
142 tropical cyclones (Gualtieri et al., 2018). Seismic noise can reveal the impact of atmospheric and  
143 oceanic conditions, providing valuable insights into weather events and climate changes (e.g.  
144 Bromirski et al. 2002; Aster et al., 2008; 2023). In particular, seismic data helps track variations  
145 in the Earth's surface caused by factors such as ocean waves, wind, and precipitation, offering a  
146 unique perspective on these phenomena (e.g. Grevemeyer et al., 2000; Borzi et al., 2022).

147 When the seismic noise is analyzed in the frequency domain, two clear peaks emerge in the  
148 spectrum (Figure 3), reflecting distinct types of ocean wave interactions (Koper et al., 2015;  
149 Ardhuin et al., 2019; Tanimoto et al., 2023). The primary peak, observed in the range of 10-20  
150 seconds (0.05-1 Hz), is generated by the impact of "swell" waves traveling in the same direction,  
151 inducing pressure variations in the Earth's crust that match the period of the waves. The secondary  
152 peak, in the range of 5-10 seconds (0.1-0.5 Hz), is produced by wind-driven waves, which  
153 propagate in different directions and generate pressure oscillations on the ocean floor (Ebeling et  
154 al., 2012). These seismic signals directly link ocean conditions with seismic activity (Li et al.,  
155 2020), providing insights into large-scale weather phenomena like ocean storms.



156

157 *Figure 3. Probabilistic Power Spectral Density (PPSD) of seismic noise for station CFR, over two years,*  
 158 *showing key sources of primary and secondary microseisms. Below, sketches illustrate the generation*  
 159 *mechanisms: primary microseisms are caused by unidirectional swell waves inducing pressure fluctuations*  
 160 *on a shoaling seafloor, while secondary microseisms result from nonlinear interactions of wind-driven*  
 161 *waves over deeper water (modified after Ebeling, 2012).*

162 Higher frequencies above 30 Hz are associated with the effects of precipitation and wind, as seen  
 163 in studies like Rindrharisaona et al. (2022) or Diaz et al. (2023). These higher-frequency seismic  
 164 signals help track more localized weather events, such as storms and heavy rainfall. Seismic data,  
 165 when integrated with other meteorological tools, enhances the ability to monitor and predict  
 166 weather events.

167 To analyse seismic data, the raw traces are first corrected for instrument response and converted  
 168 to units of velocity. These are then filtered with bandpass butterworth filters adapted to capture the  
 169 target signal: low pass filtering (<1 Hz) for wave-seafloor coupled interactions and high pass  
 170 filtering (>30 Hz) to identify possible signatures of precipitation, essentially induced pressure  
 171 fluctuations in the ground converted to weak seismic vibrations due to rain drops. Spectrograms  
 172 of these filtered seismic traces were computed using short-time Fourier transforms implemented  
 173 in the `scipy.signal` package, with the default 256-sample window length used for each segment,-to  
 174 visualise signatures of the hydro-meteorological phenomena in the frequency content of ground  
 175 vibrations.

176 Potential environmental signals in the seismic data were also investigated using power spectral  
177 density (PSD) analysis. To account for variations over time, a Probabilistic Power Spectral Density  
178 (PPSD) method was applied. The continuous waveform was divided into 1-hour time windows  
179 with 50% overlap, and a PSD was computed for each window after instrument-response correction  
180 and basic preprocessing. These estimates were combined into a probability distribution, providing  
181 a statistical overview of typical and transient noise levels across frequencies. The PPSD was  
182 produced using ObsPy (Beyreuther et al., 2010), which handles data gaps and ensures reliable  
183 normalization.

184 Temporal variations in PSD amplitudes are also analyzed to track changes in seismic noise at  
185 specific frequencies. By extracting PSD values at selected frequencies that are expected to capture  
186 primary and secondary microseisms, time series of noise levels are generated. These temporal  
187 PSDs allow for the identification of trends and correlations with environmental factors, such as  
188 ocean wave activity or weather conditions.

### 189 **3.2 Acoustic Data**

190 Infrasound waves are low-frequency acoustic waves that are inaudible to the human ear, typically  
191 below 20 Hz. These waves are generated by a variety of natural and anthropogenic sources,  
192 including meteorological events, volcanic eruptions, earthquakes, and human activities such as  
193 explosions and industrial processes (Campus, 2009; Bondár et al., 2022). In particular, infrasound  
194 is often associated with phenomena like thunderstorms, ocean waves, and large-scale atmospheric  
195 events, which generate pressure fluctuations that propagate through the atmosphere (e.g. Stopa et  
196 al., 2012; Landès et al., 2012; Listowski et al., 2022). These waves provide valuable information  
197 about the dynamics of weather systems (e.g. Hupe et al., 2019), making them an essential tool for  
198 monitoring and understanding environmental processes (e.g. Brachet et al., 2009; Hupe et al.,  
199 2022). Infrasound associated with thunderstorms, primarily generated by acoustic waves from  
200 thunder, has been studied previously and shown to be detectable at distances ranging from tens to  
201 hundreds of kilometers (e.g., Assink et al., 2008; Sindelarova et al., 2015; Šindelářová et al., 2021).  
202 Nevertheless, infrasound arrays detect signals from multiple storm-related sources, not just thunder  
203 (e.g., Waxler et al., 2024). In the present study, we build on this understanding by integrating these  
204 signals with seismic, satellite, meteorological, and water vapor observations to investigate what  
205 these complementary datasets reveal about storm evolution in a coastal environment.

206 For the monitoring of infrasound signals, we use data from an infrasound array system located at  
207 Eforie Nord-Agigea, Romania (AGIR, Figure 2). This array consists of multiple sensors, including  
208 SIS-1 infrasonic sensors (Seismowave), equipped with global positioning systems (GPS) and noise  
209 reduction technology.

210 To analyze the seismo-acoustic characteristics of the August 30-31 Black Sea storm, we used a  
211 two-pronged approach: (1) single-station signal analysis based on feature extraction and  
212 unsupervised machine learning, and (2) array-based analysis using classic multi-channel  
213 correlation algorithms. Together, these methods provide complementary insights into the acoustic  
214 behavior of the storm, capturing both local signal characteristics and spatial coherence across  
215 sensors.

216 For the single-station analysis, infrasound data recorded at the AGIR sensor (Figure 2) was  
217 segmented into 30-minute windows, and a set of time-frequency features was extracted to  
218 characterize the signal dynamics. These features describe how energy and frequency content  
219 evolve over time, providing insights into the structure of the infrasound signal. Parameters such as  
220 spectral centroid and spectral rolloff are standard descriptors in acoustic signal analysis and are  
221 suitable here because they effectively capture shifts in dominant frequency produced by lightning-  
222 generated acoustic waves or the passage of pressure disturbances, while spectral flux highlights  
223 changes in broadband acoustic energy (Pásztor et al., 2023). Spectral entropy reflects the  
224 complexity of the frequency distribution, which increases during turbulent atmospheric conditions,  
225 and the zero-crossing rate, mean, and variance of the power spectrum summarize overall activity  
226 and variability. This feature set provides a compact representation of the signal suitable for  
227 unsupervised machine-learning approaches such as clustering, techniques widely used in data  
228 mining to identify patterns in multidimensional time-frequency data (e.g., Coates and Ng, 2012),  
229 and allows us to distinguish physically interpretable stages of storm-induced changes in the  
230 infrasound wavefield.

231 The extracted features were used as input for K-Means clustering (MacQueen, 1967), an  
232 unsupervised machine learning algorithm that partitions data into a predefined number of groups,  
233 in this case, seven. K-Means minimizes within-cluster variance by iteratively assigning feature  
234 vectors to the nearest cluster centroid and updating the centroids based on the grouped data. This  
235 clustering method enables the identification of distinct acoustic patterns in the signal (e.g. Pásztor  
236 et al., 2023), offering a data-driven way to segment the storm’s infrasound profile without  
237 requiring prior labels or assumptions. The optimal number of clusters was determined using the  
238 elbow method, which evaluates within-cluster variance as a function of cluster number. To select  
239 the most informative features, we applied covariance pruning, and the temporal evolution of the  
240 features was visualized to ensure meaningful representation. This procedure resulted in six  
241 clusters, providing a balanced representation of the infrasound dynamics while avoiding over-  
242 segmentation or overfitting. By combining multiple features in the clustering, this method captures  
243 the evolving acoustic states of the storm in a compact, interpretable form.

244 In parallel with the single-station analysis, we also applied the Progressive Multi-Channel  
245 Correlation (PMCC) method, as implemented in the DTK-PMCC software (Cansi and Le Pichon,  
246 2008; Le Pichon et al., 2010) to detect and analyze coherent acoustic signals across an infrasound  
247 array. The PMCC method targets signals generated by atmospheric sources such as lightning (i.e.,  
248 associated thunders) or other pressure disturbances, operating in the low-frequency range of 0.7 to  
249 7 Hz. It is specifically suited for mini-array configurations, where signal coherence between  
250 closely spaced sensors can be exploited for precise signal detection and characterization.

251 The PMCC algorithm was implemented using a multi-resolution configuration following the  
252 standardization proposed by Garcés (2013), with window lengths and frequency bands arranged  
253 in third-octave bands. A total of 19 frequency bands were used, covering 0.1-7 Hz. Window  
254 lengths decrease logarithmically with frequency, ranging from 258 s in the lowest band to 4 s in  
255 the highest band. A 10% time step was applied (corresponding to 90% overlap between  
256 consecutive windows), and this scheme repeats every decade. Within each time-frequency  
257 segment, cross-correlations are computed between all sensor pairs to identify coherent wavefronts,  
258 signals that exhibit consistent arrival times across the array. From these detections, PMCC  
259 estimates several key propagation parameters, including back-azimuth (the direction of arrival),

260 horizontal trace velocity, amplitude, duration, and dominant frequency. This approach is  
261 particularly effective in noisy environments and enables the discrimination of storm-generated  
262 infrasound from background signals or unrelated acoustic sources. The algorithm's output consists  
263 of a time-frequency map of signal detections enriched with physical metadata, allowing for  
264 detailed interpretation of the storm's acoustic footprint and its temporal evolution.

### 265 **3.3 Satellite Observations**

266 We also incorporated data from the Meteosat Third Generation (MTG) satellite system (Holmlund  
267 et al., 2021), specifically from its Lightning Imager (LI) sensor (Viticchie et al., 2020). The MTG  
268 satellites operate in geostationary orbit at approximately 36,000 km altitude, providing continuous  
269 observations over Europe, Africa, and surrounding waters. The Lightning Imager detects cloud-  
270 to-cloud, cloud-to-ground, and intra-cloud lightning flashes using four cameras that collectively  
271 cover 86% of the Earth's visible disc from the satellite's perspective.

272 For this study, we used Level 2 group data, which includes the geographical coordinates and timing  
273 of each detected flash. By mapping these detections, we were able to analyze the spatial  
274 distribution and temporal evolution of the storm's lightning activity. The dataset also offered  
275 insights into the storm's intensity and structure, complementing other meteorological observations.

276 Associations between infrasound detections and lightning flashes detected by MTG within 50 km  
277 of the AGIR infrasound station were investigated by assuming direct-path acoustic propagation  
278 and a correspondence between infrasound time-of-arrival and the MTG lightning discharge time  
279 (after Assink et al., 2008):

$$280 \quad t = t_{\text{MTG}} + d/c + \Delta t,$$

281 where  $d$  is the distance between the lightning discharge and the infrasound station,  $c = 340\text{m/s}$ ,  
282 and  $\Delta t = \pm 10\text{s}$  accounts for timing uncertainty. Additionally, a maximum angular deviation of  $10^\circ$   
283 between the observed infrasound backazimuth and the MTG-derived backazimuth is permitted for  
284 an association to be accepted.

### 285 **3.4 GNSS Data**

286 The use of GNSS technology for atmospheric monitoring provides a powerful tool for analyzing  
287 extreme weather events. Beyond its well-known applications in navigation and timing, GNSS has  
288 become a reliable method for sensing tropospheric water vapour, an essential driver of weather  
289 systems and a key variable in forecasting models (Guerova et al., 2016; Vaquero-Martínez and  
290 Antón, 2021). Over the past two decades, ground-based GNSS networks in Europe have  
291 contributed significantly to operational meteorology by providing near real-time estimates of  
292 atmospheric water vapour, aiding in the detection and tracking of severe weather, including heavy  
293 rainfall and storms (Karabatić et al., 2011; Priego et al., 2017; Jones et al., 2020). These high-  
294 resolution observations have proven valuable for both nowcasting and validating numerical  
295 weather prediction models (Wilgan et al., 2015; Bosy et al., 2012; Awange, 2012).

296 In this study, GNSS data were collected from several networks (Figure 2), including the  
297 International GNSS Service (IGS, Johnston et al., 2017), the EUREF Permanent Network (EPN,

298 Bruyninx et al., 2012), the Romanian Position Determination System (ROMPOS, Iliescu et al.,  
299 2019), and GEOPONTICA (Dimitriu et al., 2017). A total of 37 permanent GNSS stations were  
300 analyzed over a 30-day period, with the rainiest interval selected at the midpoint of the study  
301 period. These stations provide high-quality, continuous observations critical for atmospheric  
302 monitoring.

303 The data were processed using a double-differenced, ionosphere-free combination of L1 and L2  
304 carrier phases. This approach helps minimize errors such as ionospheric delays, satellite clock  
305 biases, and other common atmospheric effects. The resulting Zenith Tropospheric Delay (ZTD)  
306 values were then corrected using the Vienna Mapping Functions 3 (VMF3, Landskron et al., 2018),  
307 which improves the accuracy of ZTD by accounting for variations in the troposphere's atmospheric  
308 conditions. Once the ZTD was refined, it was converted into integrated precipitable water vapor  
309 (PWV) using surface meteorological data (temperature and pressure) from co-located weather  
310 stations, following the method outlined by Bosy et al. (2012). This process allowed for the  
311 derivation of high-resolution atmospheric water vapor content, critical for analyzing the dynamics  
312 of the extreme storm event over the Black Sea. By combining GNSS-derived PWV with data from  
313 other observational sources, the study captured the temporal and spatial variations in atmospheric  
314 moisture, offering valuable insights into the storm's development and intensity.

### 315 **3.5 Meteorological Data**

316 To compare the infrasound signals captured during the Black Sea extreme storm event, we  
317 extracted meteorological data from the open-access ERA5 reanalysis dataset, produced by the  
318 European Centre for Medium-Range Weather Forecasts (ECMWF). This dataset provides a  
319 comprehensive record of global weather conditions from 1950 to the present (Hersbach et al.,  
320 2023). ERA5 combines observational data and advanced numerical models to generate high-  
321 resolution atmospheric parameters, including precipitation (Figure 1), wind speed, and wave  
322 height. ERA5 has been extensively validated (Jiao et al., 2021; Wu et al., 2022; Soci et al., 2024)  
323 and is widely used in studies of storm evolution and precipitation dynamics (e.g. Dullart et al.,  
324 2020; Tiberia et al., 2021; Price et al., 2025), making it a suitable choice for the mesoscale  
325 processes examined here.

326 For our study, the ERA5 data was used to track the meteorological context of the storm, offering  
327 insights into the intensity of precipitation, the evolution of wind patterns, and the development of  
328 oceanic wave heights. With high temporal (1 hour) and spatial ( $0.25^\circ \times 0.25^\circ$ ) resolution, ERA5  
329 allows for a detailed comparison of the storm's meteorological characteristics over time. These  
330 comparisons help us understand the storm's dynamics and assess its impact, further enhancing the  
331 interpretation of infrasound signals and aiding in future storm prediction and monitoring efforts.  
332 The open-access nature of ERA5 ensures broad accessibility, contributing to the transparency and  
333 reproducibility of our storm analysis (Copernicus Climate Change Service, Climate Data Store,  
334 2023).

335

336

337

338 **4. Results**

339 **4.1 Seismic signatures of storm evolution**

340 High frequency (>30 Hz) analysis of seismic noise reveals strong signals during periods of intense  
341 rainfall (Figure 4). Specifically, the displacement envelope at station MANR and its spectrogram  
342 for 30 August, 12:00 UTC to 31 August, 06:00 UTC (Figures 4b, c) reveal strong signal around  
343 midnight, when recorded precipitation exceeded 20 mm per 10 minutes. Similar temporal patterns  
344 in the seismic spectrogram were also visible when compared with hourly precipitation levels from  
345 ERA5, indicating that the high amplitude of energy observed above 30 Hz is most plausibly  
346 generated by raindrop impacts.

347 However, this correspondence is not uniform across all rainfall episodes. While the main  
348 precipitation maximum on 30-31 August produces a clear and sustained seismic response, several  
349 lower-intensity precipitation pulses show a much weaker or no recognizable signature in either the  
350 seismic envelope or spectrogram. This behaviour is consistent with previous work (e.g.,  
351 Rindraharisaona et al., 2022), which demonstrates that only rainfall above a certain intensity, or  
352 involving sufficiently large drops, generates impact forces strong enough to be detected by  
353 broadband seismometers. Our observations therefore reflect both strong positive correlations  
354 during intense rainfall and the lack of seismic expression for weaker precipitation. This selective  
355 sensitivity supports the interpretation that high-frequency seismic noise can reliably track strong  
356 rainfall peaks but is less responsive to light or moderate precipitation, an important nuance when  
357 interpreting multi-sensor relationships in this study.

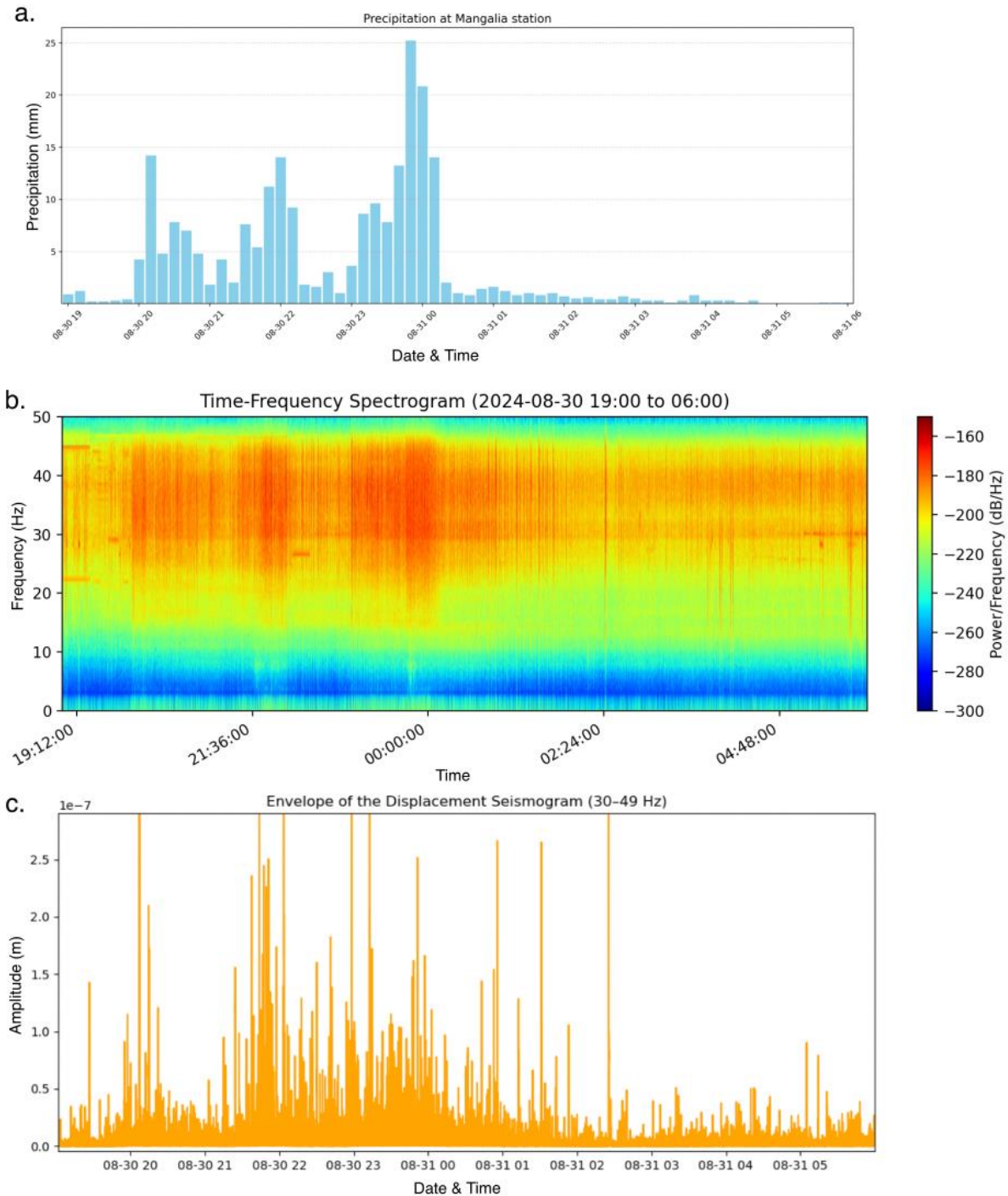
358 Anthropogenic seismic noise is typically strongest at low to mid frequencies (<25 Hz), where day-  
359 night variations reflect traffic, human activity, and transient signals from machinery, while higher-  
360 frequency bands (25-45 Hz) may include periodic contributions from rotating equipment (e.g.,  
361 Gross & Ritter, 2008; Diaz et al., 2017). The bandwidth targeting rainfall in this case is between  
362 30-50 Hz, which is above the dominant frequency content of most anthropogenic sources and  
363 overlaps with raindrop-impact energy documented in recent rainfall-seismic studies.

364

365

366

367

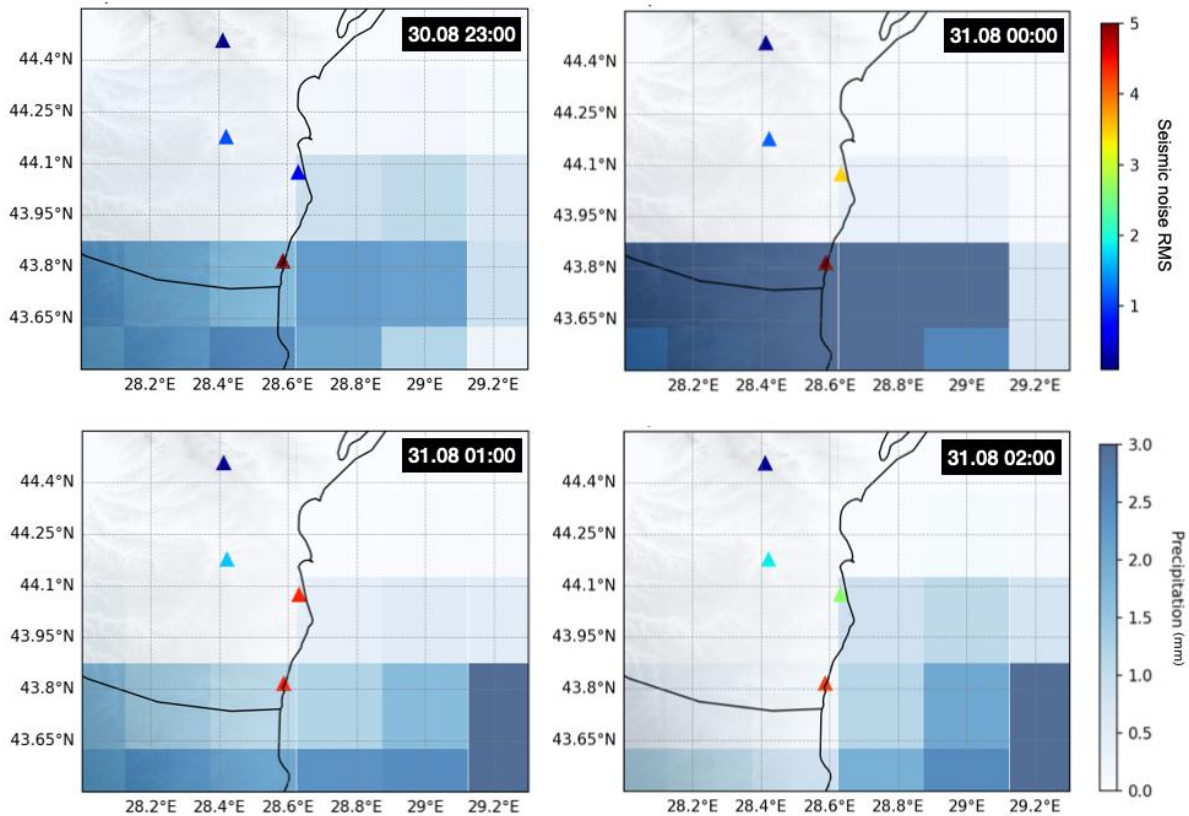


368

369 *Figure 4. High frequency (30-50Hz) observations of the storm at station MANR. a. Time series of total*  
 370 *precipitation every 10 minutes from the ANM station at Mangalia b. Spectrogram of the seismic time series*  
 371 *for station MANR. c. Envelope of the displacement seismogram at station MANR.*

372 To visualise the signature of the storm passing over the network of broadband seismic stations in  
 373 the coastal area, we also plotted the hourly precipitation values with the hourly root-mean-square  
 374 amplitudes of the high-frequency (>30 Hz) seismic velocity envelopes recorded at seismic stations.

375 Figure 5 shows three snapshots of hourly plots of gridded precipitation data from ERA5, which  
 376 have a lower amplitude than point measurements at the Mangalia station, due to the averaging over  
 377 the grid block. This figure presents a temporal coincidence between changing precipitation patterns  
 378 from ERA5 data and the amplitudes of high-frequency seismic noise. This observation further  
 379 supports the likelihood of a causal relationship. These high-frequency seismic signals could  
 380 potentially be monitored in near real time to flag intense rainfall events, providing a conceptual  
 381 basis for a simple streaming detection approach.



382

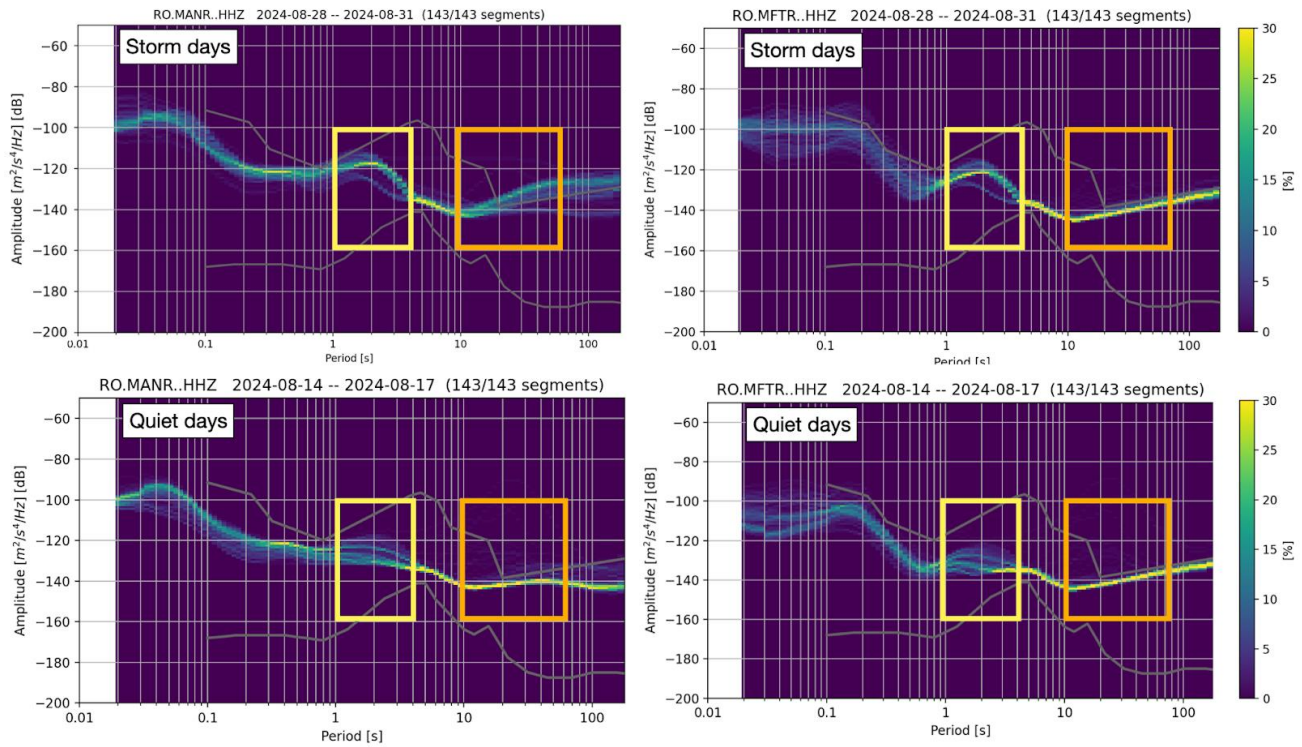
383 *Figure 5. Distribution of hourly RMS of high pass filtered (>30 Hz) seismograms and precipitation data.*  
 384 *Colours indicate hourly RMS amplitude of velocity envelopes filtered 30-50 Hz. Background coloured*  
 385 *grid indicates the total precipitation (mm) from ERA5 data.*

386 The analysis of the microseismic noise frequency band is closely linked to the interaction between  
 387 ocean waves and the seafloor, which is influenced by storm conditions. To assess the storm's  
 388 impact, we analyze the PPSD (Probabilistic Power Spectral Density) of noise recorded at several  
 389 stations during both storm and quiet days, using the latter as a baseline. Figure 6 shows examples  
 390 of PPSD at stations MANR and MFTR (Figure 2), revealing differences in PSD amplitudes across  
 391 the primary and secondary microseismic bands. These differences indicate the presence of high-  
 392 intensity wind-driven waves and swell energy in the sea.

393 The secondary microseismic band, in particular, shows a significant rise in amplitude during  
 394 storms, driven by wind-induced pressure fluctuations in the shoaling seafloor (Figure 3, Ebeling  
 395 et al., 2012). On quiet days, the PSD remains consistently lower, typically staying below the -120

396 dB threshold. This stark contrast emphasizes the role of atmospheric conditions in modulating  
 397 seismic noise, with storms causing a notable increase in energy across both frequency bands. The  
 398 temporal evolution of the PSD values (Figure 7) further highlights the storm's impact, with  
 399 fluctuations corresponding to changes in environmental factors, reinforcing the connection  
 400 between storm activity and the observed seismic signals.

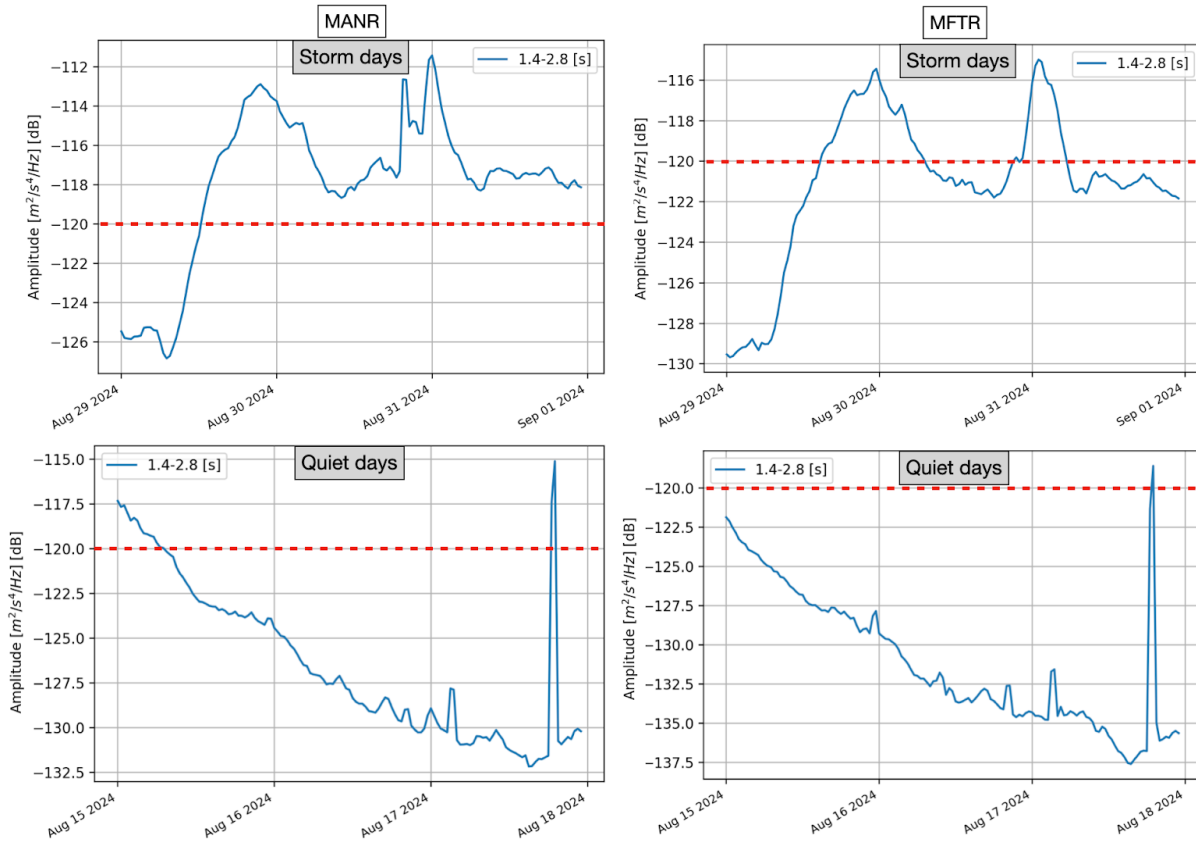
401



402

403 *Figure 6. Probabilistic Power Spectral Density (PPSD) plots for two seismic stations near the Black Sea*  
 404 *coast capturing the target storm signal in the microseismic bandwidths (marked with rectangles). The top*  
 405 *panels show the PPSD distributions across frequencies, indicating the probability of power spectral*  
 406 *density values in percentage for days including the Black Sea storm. The bottom panels show PPSD for*  
 407 *days with no recorded events.*

408 Anthropogenic seismic noise does not significantly affect the microseismic band (0.1-1 Hz).  
 409 Human-generated vibrations predominantly occupy frequencies above 1 Hz, while long-period  
 410 microseisms are produced by ocean wave interactions and are coherent over large distances. The  
 411 temporal evolution of the microseismic energy observed in this study matches changes in wave  
 412 state associated with the storm rather than any local activity. Similar to the findings of Gross &  
 413 Ritter (2009), the sub-Hz frequency range is dominated by natural sources, with anthropogenic  
 414 contributions being negligible.



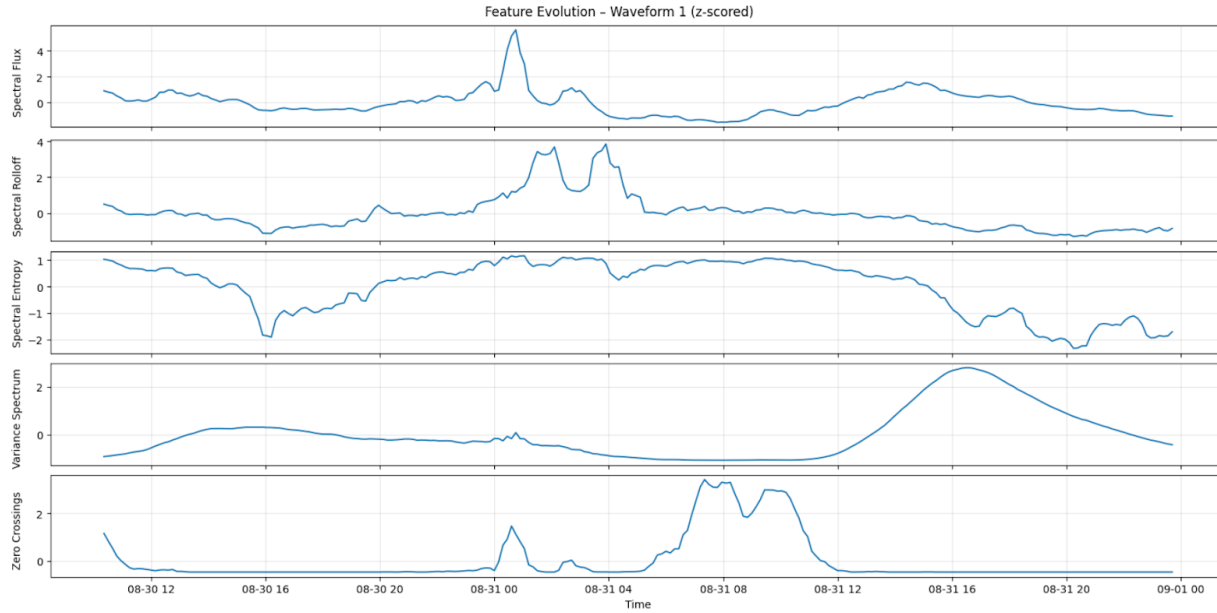
415

416 *Figure 7. Temporal PSDs for two seismic stations near the Black Sea Coast in the secondary*  
 417 *microseismic band showing significantly higher values ( $>-120$  dB) during stormy days compared to days*  
 418 *without recorded precipitation.*

## 419 4.2 Infrasound and satellite lightning observations

### 420 4.2.1 Single-station feature extraction

421 The evolution of time-frequency features over the duration of the Black Sea storm revealed distinct  
 422 patterns in the infrasound signal (Figures 8 and 9). Centroid and rolloff show parallel behavior  
 423 because they are both frequency-domain descriptors tied to the distribution of spectral energy, and  
 424 so both respond strongly to the same uplift in energy during the storm's peak. Spectral flux, by  
 425 contrast, quantifies inter-frame spectral change, so its peak occurs where the spectrum transitions  
 426 most rapidly, even when that does not coincide with the maximum absolute energy (e.g. Pásztor  
 427 et al., 2023). Finally, the zero-crossing rate reflects time-domain volatility, not spectral shape,  
 428 which explains its distinct pattern, such as the storm's later stages may introduce broadband  
 429 turbulence or noise components that boost zero crossings independently of the spectral shifts  
 430 visible in the first two panels. While the individual features varied over time, it is the combination  
 431 of these features through K-means clustering that effectively identifies the time frame  
 432 corresponding to the main precipitation episode. Zero-crossings exhibited more variable patterns,  
 433 reflecting high-frequency fluctuations, but the joint clustering of all features robustly captures the  
 434 timing of the storm's most intense phases.

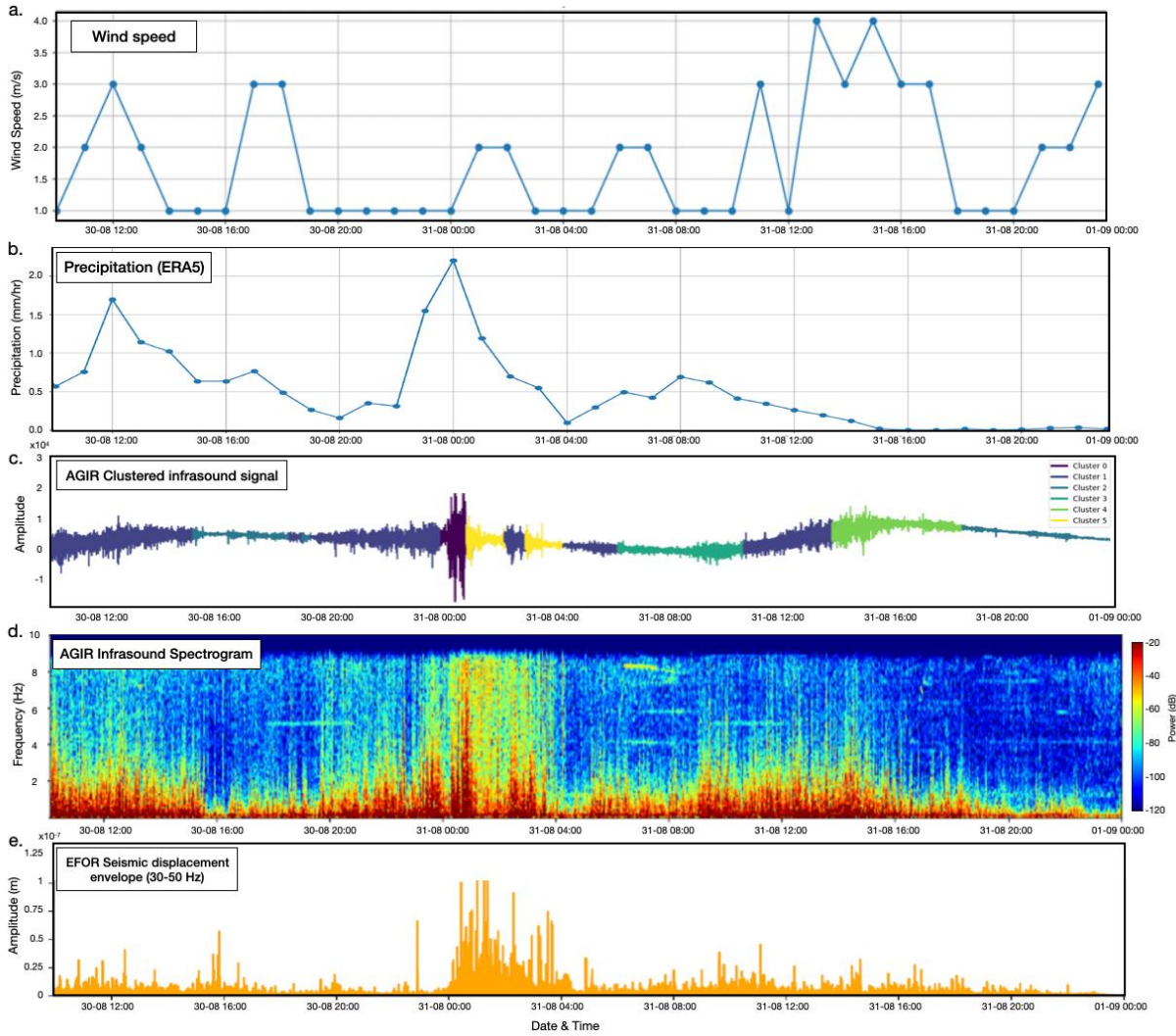


435

436 *Figure 8. Time-frequency feature analysis for the single-station infrasound signal recorded at AGIR during*  
 437 *the Black Sea Storm.*

438 K-means clustering separated the acoustic data into six groups with distinct spectral and amplitude  
 439 characteristics (Figure 9). These clusters highlight acoustic states that may relate to different  
 440 environmental conditions during the monitoring period. For example, Cluster 0 coincides with  
 441 periods of intense precipitation and stronger winds, while Cluster 1 captures intervals with  
 442 moderate amplitudes but persistently elevated background acoustic levels, without corresponding  
 443 rainfall or wind peaks. Cluster 2 reflects calmer conditions with low amplitudes and little or no  
 444 precipitation. Transitional patterns also arise, such as Cluster 3, which appear before intervals  
 445 grouped in Cluster 1 and mark intermediate acoustic activity. Overall, the clustering approach  
 446 demonstrates that combining multiple features reveals consistent acoustic regimes and can help  
 447 differentiate environmental conditions, without relying on any single parameter.

448 Interestingly, the spectral content of the infrasound signal showed similarities to seismic signal  
 449 envelopes, particularly in the high frequency ranges (Figure 9), which may suggest a connection  
 450 between the atmospheric pressure waves detected by infrasound and the ground vibrations  
 451 captured by seismic instruments. This overlap implies that both seismic and infrasound signals  
 452 could be complementary in capturing different aspects of storm dynamics, with seismic signals  
 453 reflecting ground vibrations and infrasound capturing the atmospheric processes.



454

455 *Figure 9. Clustering results of infrasound signals recorded at AGIR from the August Black Sea storm event*  
 456 *compared with precipitation data and seismic signal from EFOR station. a. Wind speed per hour measured*  
 457 *at ANM meteorological station Constanta; b. Average precipitation data from 1°x1° around AGIR. c. Raw*  
 458 *infrasound signal recorded at the AGIR sensor during the period of August 30-31, 2024, with different*  
 459 *segments color-coded according to the cluster they belong to, based on K-means clustering of 30-minute*  
 460 *time-frequency feature windows. d. The corresponding spectrogram, generated using Blackman windowing*  
 461 *with 128 samples and 70% overlap; e. Seismic displacement envelope at station EFOR, filtered between*  
 462 *30-50 Hz.*

463

464

465

466

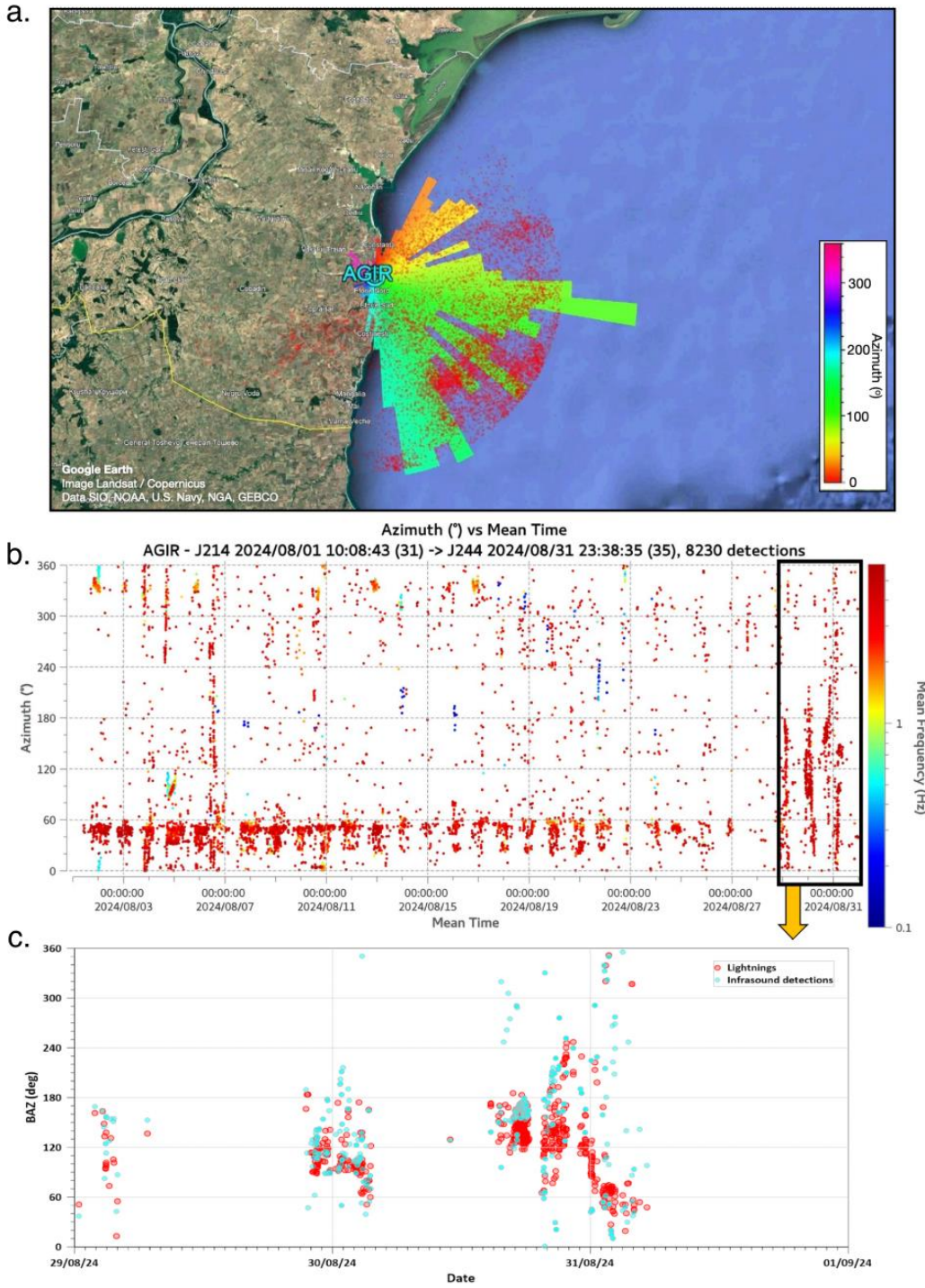
467

## 468 4.2.2 Array analysis and lightning detection

469 The PMCC algorithm allowed us to isolate coherent infrasound signals and estimate their  
470 propagation parameters, such as back-azimuth and arrival times, across the sensor network. Nearly  
471 11,000 lightning flashes were detected by the MTG Lightning Imager within 50 km of the AGIR  
472 station during the Black Sea storm (Figure 10A), providing a dense reference set for comparison.  
473 Within the relevant 0.6-7 Hz frequency band, approximately 1,100 infrasound detections were  
474 identified. These signals primarily consisted of long-duration wave trains with frequent amplitude  
475 peaks and short-lived disturbances characteristic of lightning-generated infrasound. Their  
476 dominant frequency was around 3 Hz, and amplitudes ranged from 0.01 to 3.4 Pa (Figure 10b).

477 A subset of the infrasound detections could be confidently associated with individual lightning  
478 discharges based on temporal alignment and backazimuth consistency. Overall, we were able to  
479 associate 6.4% of lightning flashes with infrasound detections at AGIR (Figure 10c). This level of  
480 correspondence is reasonable given that only a subset of lightning discharges radiate infrasound  
481 efficiently and that propagation strongly depends on altitude, source geometry, and atmospheric  
482 conditions. Nevertheless, these coincident detections demonstrate that lightning-generated  
483 infrasound was clearly recorded during the storm and that the PMCC-derived acoustic signatures  
484 provide valuable insight into the evolution of electrical activity and storm dynamics.

485 Anthropogenic noise sources, such as wind turbines (e.g., Jakobsen, 2005), industrial machinery  
486 (Gastmeier and Howe, 2008), and road traffic (Grafkina et al., 2019), are well-documented  
487 challenges for infrasound studies because they often generate persistent, periodic, or tonal signals  
488 that can mask natural atmospheric phenomena. The AGIR infrasound array used here is located in  
489 a semi-rural setting, distant from major roads and industrial facilities, which reduces the likelihood  
490 of local anthropogenic contamination. Several independent lines of evidence indicate that such  
491 contamination is negligible in this case study. First, the strongest infrasound signatures occurred  
492 during night-time hours, when human activity is minimal. Second, both the clustering and PMCC  
493 analyses identify transient signals with energy peaking around  $\sim 3$  Hz, which contrasts sharply with  
494 the more continuous or harmonic spectral patterns typically produced by anthropogenic sources.  
495 Third, the temporal alignment of these acoustic signatures with independent observations of  
496 lightning and precipitation provides strong confirmation that the detected infrasound variability is  
497 storm-related rather than anthropogenic in origin.



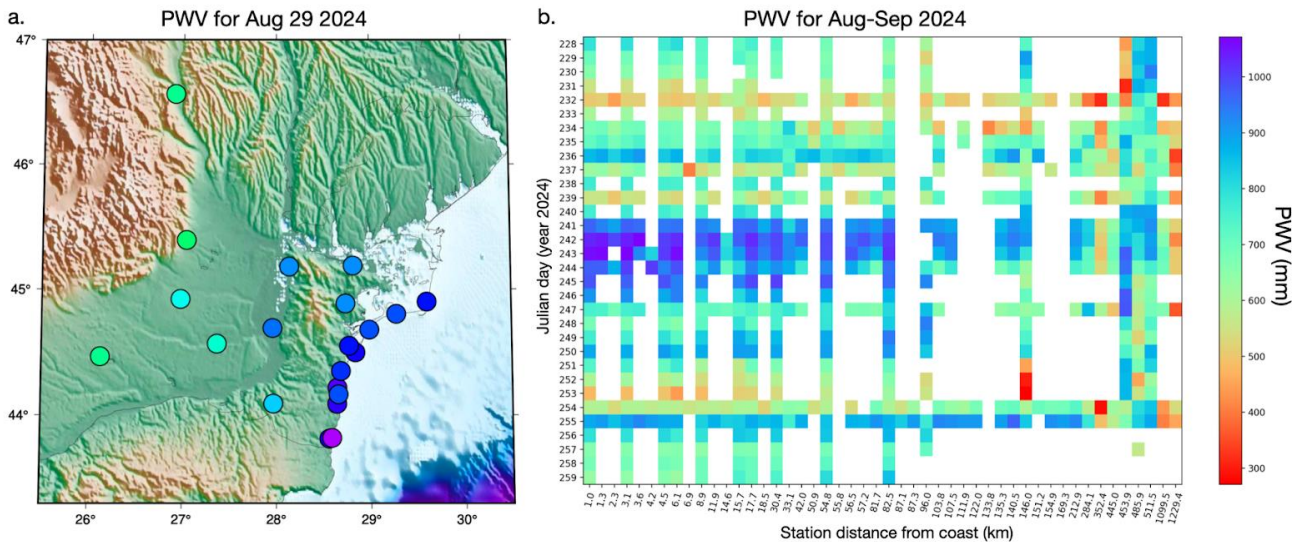
498

499 *Figure 10. a. Polar histogram of infrasound detections from the AGIR station, displayed with © Google*  
 500 *Earth, along with the locations of lightning strikes detected by the MTG Lightning Imager system for the*  
 501 *period from 29-31st of August 2024. The geographical position of the AGIR infrasound station is also*  
 502 *shown on the map. b. diagram of high-frequency detections from the AGIR infrasound station between 1-*  
 503 *31st of August 2024. c. Associations between events detected by the AGIR infrasound array and the MTG*  
 504 *satellite database for 29-31st of August 2024.*

505 **4.3 GNSS-derived precipitable water vapor trends**

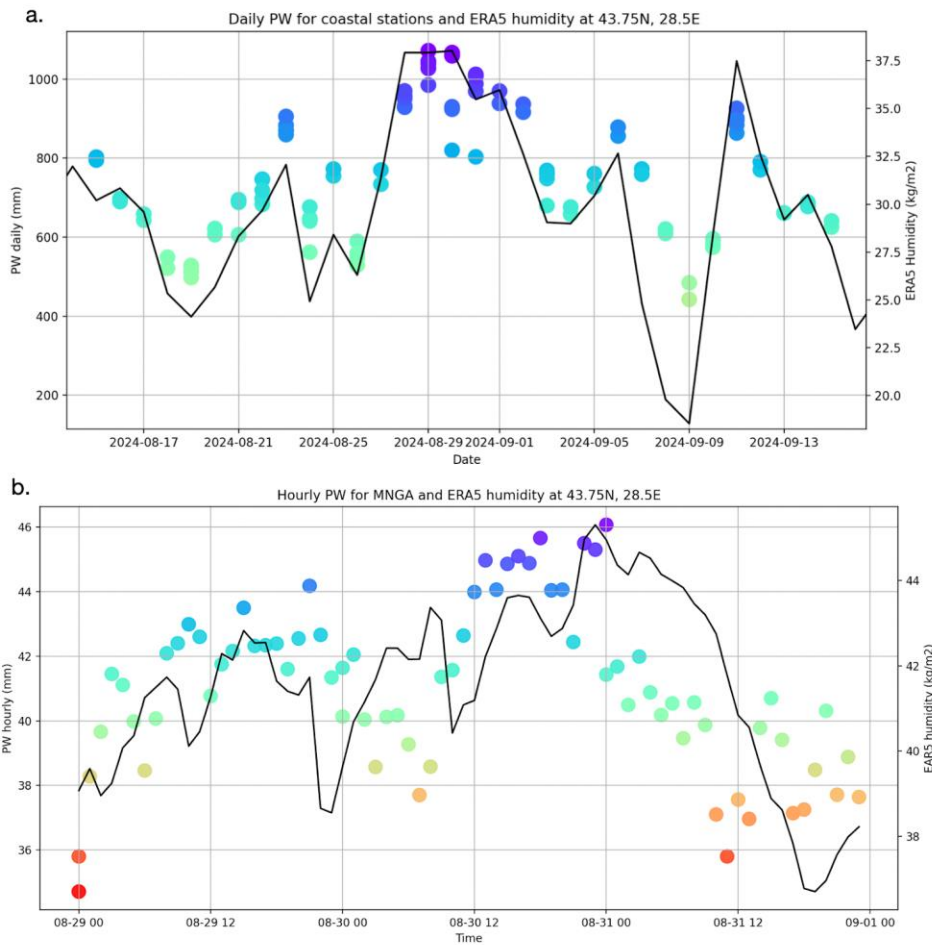
506 The analysis of daily GNSS-derived precipitable water vapor (Figure 11) reveals clear temporal  
507 variations, with the highest PWV values consistently recorded on stormy days (>900 mm per day  
508 on DOY 240-243, i.e. August 27-30). Notably, the peak values occurred between DOY 241 and  
509 DOY 243 (Figure 11b), when the heaviest rainfall was observed (Figure 1). Coastal stations  
510 showed extremely high PWV values (>950 mm per day) compared to inland stations (>800 mm  
511 per day), with a slight decrease in PWV away from the coast (Figure 11a). This spatial distribution  
512 highlights the geographical gradient of atmospheric moisture, with the highest PWV  
513 concentrations near coastal areas, also decreasing gradually toward the north away from the storm  
514 peak. Interestingly, some inland stations (BUCU, PGNL, RMSR) recorded their peak PWV on  
515 DOY 255, corresponding to the onset of the Boris storm, another significant extreme rainfall event  
516 that swept through Central and Eastern Europe (Athanas et al., 2024).

517 Elevated PWV was observed as early as August 27th (Figure 12a), suggesting that the tropospheric  
518 moisture loading began to increase several days before the onset of the rainfall. This accelerated  
519 increase in PWV can serve as an early indicator of a developing weather system. Remarkably,  
520 although HAR1, located inland, did not directly experience the extreme rainfall, it exhibited  
521 similar PWV behavior to coastal stations, suggesting that GNSS stations, even outside the  
522 immediate storm zones, can capture atmospheric signals indicative of intense precipitation. This  
523 finding offers a valuable precedent, showing that PWV measurements at GNSS stations not  
524 directly in the storm path can still provide critical insights into moisture dynamics at the  
525 tropospheric level. The comparison with ERA5’s total-column water vapour further supports this  
526 interpretation, as the broad temporal evolution of ERA5 humidity mirrors the GNSS-derived daily  
527 PWV patterns, despite the inherently coarser resolution of the reanalysis data.



528  
529 *Figure 11. a: Map of GNSS stations coloured as a function of PWV estimated for the 29th of August. b.*  
530 *Daily PWV values for each station, plotted as a function of their longitudinal distance relative to the city*  
531 *of Constanta.*

532 Using the hourly PWV data, Figure 12b illustrates the evolution of water vapour at the MNGA  
 533 station, which recorded the heaviest rainfall in the study area. Notably, MNGA also showed a rapid  
 534 buildup of PWV, reaching values greater than 44 mm/hr just a few hours before the storm event.  
 535 This rapid increase in PWV strongly suggests that the accumulation of atmospheric moisture is a  
 536 precursor to extreme weather events, such as intense rainfall and storms. This observation aligns  
 537 with known atmospheric dynamics, where a significant increase in water vapor content precedes  
 538 heavy precipitation, providing further evidence of the potential for GNSS-based PWV monitoring  
 539 to serve as an early warning tool for extreme weather. The general rising trend toward the event is  
 540 present in both GNSS-based and ERA5 reanalysis datasets, although some minor fluctuations are  
 541 not matched. After the storm, the GNSS PWV drops sharply while ERA5 maintains elevated  
 542 values for several hours. These differences show that GNSS can resolve rapid, real-time  
 543 atmospheric changes that may be blurred in large-scale weather model products.



544  
 545 *Figure 12. Comparison of GNSS-derived precipitable water vapor (coloured circles) with independent*  
 546 *humidity data (black line) from ERA5's total column vertically integrated water vapor parameter. a. Daily*  
 547 *PWV values at selected GNSS stations (CONB, HARI, MNGA, MNGL, MNGM, TUZL) alongside daily*  
 548 *averaged ERA5 humidity. b. Hourly PWV values at the MNGA GNSS station compared with hourly ERA5*  
 549 *humidity at the 43.75°N, 28.5°E grid point.*

550

551 **5. Discussion**

552 Storm evolution, in the meteorological sense, describes the sequence of processes from pre-storm  
553 atmospheric moisture accumulation to convective initiation, peak rainfall, electrical activity, and  
554 the associated marine response along coastal areas. The multi-sensor dataset used here captures  
555 these different stages: GNSS-PWV documents the build-up of column water vapor before  
556 convective onset, infrasound detects lightning-generated acoustic waves and pressure disturbances  
557 during the mature convective phase, high-frequency seismic noise reflects the timing and spatial  
558 progression of intense rainfall at the surface, microseisms respond to storm-driven changes in sea  
559 state, and ERA5/MTG provide the mesoscale structure that ties these geophysical signals together.  
560 By observing the same storm through these complementary physical pathways, we can outline a  
561 more detailed picture of how the storm developed, intensified, and decayed than is possible from  
562 individual datasets.

563 The integration of infrasound, seismic, and GNSS data in monitoring the extreme storm event over  
564 the Black Sea provides valuable insights into the dynamics of storm behavior and demonstrates  
565 the potential of repurposing non-conventional sensors for meteorological analysis. Infrasound  
566 data, for instance, revealed a clear acoustic signature of lightning activity, with signals detected in  
567 the range of 0.6 to 7 Hz corresponding to electrical discharges. The high frequency of infrasound  
568 detections (around 1,100) supports its utility as a reliable tool for tracking storm-related  
569 phenomena, particularly lightning, which is difficult to capture with traditional methods. However,  
570 the signals did not always perfectly align with lightning strikes, indicating that other factors, such  
571 as the movement of storm systems or variations in atmospheric conditions, may influence  
572 infrasound signatures. This suggests that refining the correlation between infrasound signals and  
573 lightning activity could be an avenue for future research, particularly in cases of sparse lightning  
574 or in remote regions.

575 Seismic data alone also showed a strong connection between high-frequency seismic noise and  
576 heavy rainfall, supporting previous studies that linked seismic signals to rainfall intensity. The  
577 distinction between high-frequency and low-frequency seismic noise is particularly noteworthy.  
578 Increases in high-frequency seismic noise occurred during intense precipitation, while low-  
579 frequency signals were associated with wave height and storm-driven winds. This suggests that  
580 different seismic frequencies capture distinct storm dynamics, with high-frequency signals  
581 reflecting localized rainfall impacts and low-frequency signals tied to broader atmospheric and  
582 oceanic interactions. This dual-frequency approach provides a more nuanced interpretation of  
583 seismic data in storm monitoring, highlighting its complexity.

584 A key finding of this study is that K-means clustering of multiple acoustic features, including  
585 spectral centroids, roll-off, flux, and zero-crossing rate, effectively segmented the infrasound  
586 record into distinct storm phases. This approach proved more robust than relying on any single  
587 feature, as the combination captured the complex, evolving nature of the storm's acoustic signature.  
588 For instance, the identified clusters delineated periods of intense precipitation, elevated  
589 background acoustic levels, and calm intervals, providing a data-driven overview of the storm's  
590 progression. The fact that these acoustically defined phases align with independent meteorological  
591 observations, such as rainfall peaks, confirms that the infrasound signal variability is a direct  
592 response to the storm's atmospheric dynamics.

593 Furthermore, the observed spectral similarity between the infrasound signals and high-frequency  
594 seismic envelopes suggests a coupled seismo-acoustic response to the storm. This implies that the  
595 same atmospheric forcing, such as pressure fluctuations from rainfall and wind, generates  
596 complementary signals in the atmosphere (infrasound) and the ground (seismic waves). Our  
597 findings are consistent with other studies of intense weather systems, where coupled microbarom-  
598 microseism signals have been shown to track storm structure and evolution (e.g., Butler & Aucan,  
599 2018; Smirnov, 2021). The coherent acoustic and seismic responses to atmospheric-oceanic  
600 pressures, as also documented in Distributed Acoustic Sensing studies (Taweessintananon et al.,  
601 2023) and surf studies (Francoeur et al., 2025), reinforce the interpretation of a shared source  
602 mechanism. Therefore, a major and logical next step is to move beyond analyzing these datasets  
603 in parallel and to perform joint clustering of seismo-acoustic data (e.g. Floroiu et al., 2025). Such  
604 an integrated approach could unlock a more comprehensive, multi-physics understanding of storm  
605 dynamics by simultaneously characterizing the coupled atmospheric and ground-borne wavefields.

606 The temporal variations observed in GNSS-derived integrated precipitable water vapor provide  
607 valuable insights into atmospheric moisture dynamics before extreme weather events. The  
608 pronounced increase in PWV, particularly in the days leading up to and during the storm, supports  
609 the link between elevated atmospheric water vapor and precipitation. Notably, the PWV buildup  
610 starting roughly three days before the extreme rainfall suggests that rising moisture levels in the  
611 troposphere can serve as an early indicator of impending intense precipitation. Even stations  
612 located up to 130 km inland, such as HAR1, recorded similar PWV trends, indicating that GNSS  
613 stations outside direct storm zones can still provide crucial atmospheric data. Hourly PWV trends  
614 further revealed a rapid increase several hours before precipitation, with values exceeding 44  
615 mm/hr, highlighting the accumulation of moisture just before heavy rainfall. These findings align  
616 with the notion that increasing atmospheric moisture acts as a precursor to intense precipitation,  
617 highlighting the potential of GNSS-based PWV monitoring as a real-time tool for tracking  
618 moisture and understanding short-term atmospheric fluctuations.

619 The integration of GNSS, infrasound, and seismic data provides a more comprehensive  
620 understanding of storm dynamics than any single data source alone. The synergy between these  
621 diverse sensor types allows for the detection of atmospheric moisture, lightning activity, rainfall-  
622 induced seismic signals, and storm-driven oceanic interactions. Future research should focus on  
623 refining unsupervised learning algorithms for infrasound and seismic signal classification,  
624 optimizing joint clustering techniques, and improving the integration of these data sources to  
625 enhance storm forecasting and early-warning systems. We believe this multi-sensor approach  
626 holds promise for improving our ability to predict extreme weather events, understand their  
627 impacts, and mitigate associated risks.

## 628 **6. Conclusions**

629 This study presents a comprehensive analysis of a record-breaking storm over the Black Sea, using  
630 a combination of GNSS, infrasound, and seismic data to capture the dynamics of extreme weather  
631 events. Our findings underscore the power of multi-sensor networks in enhancing the  
632 understanding of storm behavior, particularly in the context of atmospheric moisture, lightning  
633 activity, and storm-induced seismic signals. GNSS-derived integrated precipitable water vapor  
634 indicates a clear buildup of atmospheric moisture hours before the onset of heavy rainfall,  
635 providing valuable insights into the lead-up to extreme precipitation events. Infrasound and

636 seismic data further complemented this analysis, with infrasound serving as a reliable tool for  
637 tracking lightning activity and seismic data revealing the link between rainfall intensity and high-  
638 frequency seismic noise.

639 The storm we analyzed is not only a significant meteorological event but also serves as a powerful  
640 example of how climate change may be influencing the frequency and intensity of extreme weather  
641 phenomena. Record-breaking storms like this are increasingly being recognized as evidence of  
642 shifting atmospheric conditions, driven by global climate change. The integration of GNSS,  
643 infrasound, and seismic data provides a more nuanced and holistic view of storm dynamics,  
644 highlighting the need for advanced monitoring systems to predict and respond to such extreme  
645 events. Moving forward, the combination of these innovative tools holds great potential for  
646 improving early-warning systems, enhancing storm forecasting, and better understanding the  
647 impacts of climate change on atmospheric and oceanic processes.

## 648 **7. Code availability**

649 Seismic data were processed with the open-source python framework for seismology Obspy  
650 (Beyreuther et al., 2010). Infrasound data was processed with the WinPMCC software (Le Pichon  
651 et al., 2010) developed by CEA/DASE (French Atomic Energy Commission, Environmental  
652 Assessment and Monitoring Department) and open-source Python libraries for signal processing.  
653 Some of the figures were made with GMT (Generic Mapping Tools, Wessel et al., 2019). The  
654 GNSS data was processed using Gamit/Globk (Herring et al., 2020) developed by Massachusetts  
655 Institute of Technology (<http://www-gpsg.mit.edu/gg/>).

## 656 **8. Data availability**

657 Seismic data are part of the Romanian National Seismic Network maintained by the National  
658 institute for Earth Physics (NIEP, [www.infp.ro](http://www.infp.ro)) and are freely available in the miniseed format via  
659 EIDA (European Integrated Data Archive, <https://www.orfeus-eu.org/data/eida/>). GNSS data are  
660 available for download from NIEP (<http://gps.infp.ro/#/download>) and are provided in the  
661 standardized RINEX v2 format, with 24-hour files sampled at 30-second intervals. Infrasound data  
662 at AGIR are available to download from NIEP via FDSN dataselect web service. Hourly hydro-  
663 meteorological data were obtained from the Copernicus Climate Change Service, Climate Data  
664 Store (<https://doi.org/10.24381/cds.bd0915c6>), ERA5 dataset (Hersbach et al., 2023). Limited  
665 wind and precipitation data were downloaded from the National Meteorological Agency from  
666 <https://www.meteoromania.ro/grafice/> (accessed on 13.09.2024) and from  
667 [https://www.meteoromania.ro/clim/caracterizare-lunara/cc\\_2024\\_08.html](https://www.meteoromania.ro/clim/caracterizare-lunara/cc_2024_08.html) (accessed on  
668 10.11.2025), respectively. Lightning data came from Meteosat Third Generation Lightning Imager  
669 operated by EUMETSAT (The European Organisation for the Exploitation of Meteorological  
670 Satellites, <https://www.eumetsat.int/>).

671

## 672 **9. Author contribution**

673 **Laura Petrescu:** Conceptualization, Methodology, Software, Formal analysis, Data Curation,  
674 Writing-Original Draft, Visualization; **Bogdan Antonescu:** Conceptualization, Writing-Review &

675 Editing, Visualization; **Sorin Nistor**: Software, Formal Analysis, Data curation, Visualisation,  
676 Writing-Review & Editing; **Iustin Floroiu**: Methodology, Software, Formal analysis, Data  
677 Curation, Writing-Original Draft, Visualization; **Dragoş Ene**: Software, Formal analysis, Data  
678 Curation, Writing-Review & Editing; **Daniela Ghica**: Software, Formal analysis, Data Curation;  
679 **Constantin Ionescu**: Funding Acquisition, Resources, Project administration; **Andrei Anghel**:  
680 Methodology, Supervision; **Mihai Datcu**: Methodology, Supervision, Funding Acquisition,  
681 Resources, Project administration.

## 682 **10. Acknowledgments**

683 We would like to thank the technicians and staff at NIEP for their support in installing,  
684 maintaining, and ensuring the proper functioning of the equipment used in this study. Additionally,  
685 we appreciate the efforts of those involved in data formatting and preparation (Cristian Neagoe,  
686 Eduard Nastase, Victorin Toader) which were essential for this work. We also thank the two  
687 anonymous reviewers for their valuable feedback, which helped improve the manuscript.

## 688 **11. Financial support:**

689 This work was carried out in the framework of the “Competence Center for Climate Change Digital  
690 Twin for Earth forecasts and societal redressment” Project PNRR- DTEClimate nr.  
691 760008/31.12.2023, subproject Reactive “The Research center for climate change due to natural  
692 disasters and extreme weather events”, supported by the Ministry of Research, Innovation and  
693 Digitalization of Romania.

## 694 **12. References**

695 Antonescu, B., Dafis, S., & Faranda, D.: Changes in precipitation patterns driving August 2024  
696 Romania floods mostly driven by human-driven climate change. *ClimaMeter, Institut Pierre*  
697 *Simon Laplace, CNRS*. <https://doi.org/10.5281/zenodo.14056214>, 2018.

698 Ardhuin, F., Gualtieri, L., Stutzmann, E., Nakata, N. and Fichtner, A.: Physics of ambient noise  
699 generation by ocean waves. In *Seismic ambient noise*, Eds: Nakata, N., Gualtieri, L., Fichtner, A.  
700 Cambridge University Press, 69-108, <https://doi.org/10.1017/9781108264808.005>, 2019.

701 Assink, J. D., Evers, L. G., Holleman, I., and Paulssen, H.: Characterization of infrasound from  
702 lightning, *Geophysical Research Letters*, 35, L15802, <https://doi.org/10.1029/2008GL034193>,  
703 2008.

704 Aster, R.C., McNamara, D.E. & Bromirski, P.D.: Multidecadal climate-induced variability in  
705 microseisms. *Seismological Research Letters*, 79(2), 194-202,  
706 <https://doi.org/10.1785/gssrl.79.2.194>, 2008.

707 Aster, R.C., Ringler, A.T., Anthony, R.E., & Lee, T.A.: Increasing ocean wave energy observed  
708 in Earth’s seismic wavefield since the late 20th century. *Nature Communications*, 14(1), 6984,  
709 <https://doi.org/10.1038/s41467-023-42673-w>, 2023.

- 710 Athanase, M., Sánchez-Benítez, A., Monfort, E., Jung, T. and Goessling, H.F.: How climate  
711 change intensified storm Boris' extreme rainfall, revealed by near-real-time storylines.  
712 *Communications Earth & Environment*, 5(1), 676, <https://doi.org/10.1038/s43247-024-01847-0>,  
713 2024.
- 714 Awange, J.L.: Environmental monitoring using GNSS: Global navigation satellite systems,  
715 Springer, Heidelberg, <https://doi.org/10.1007/978-3-540-88256-5>, 2012.
- 716 Beyreuther, M., Barsch, R., Krischer, L., Megies, T., Behr, Y. and Wassermann, J.: ObsPy: A  
717 Python toolbox for seismology. *Seismological Research Letters*, 81(3), 530-533,  
718 <https://doi.org/10.1785/gssrl.81.3.530>, 2010.
- 719 Bengtsson, L., Hodges, K.I. and Roeckner, E.: Storm tracks and climate change. *Journal of*  
720 *climate*, 19(15), 3518-3543, <https://doi.org/10.1175/JCLI3815.1>, 2006.
- 721 Bollinger, L., Perrier, F., Avouac, J.P., Sapkota, S., Gautam, U., Tiwari, D.R.: Seasonal  
722 modulation of seismicity in the Himalaya of Nepal, *Geophysical Research Letters*, 34(8),  
723 <https://doi.org/10.1029/2006GL029192>, 2007.
- 724 Bondár, I., Šindelářová, T., Ghica, D., Mitterbauer, U., Liashchuk, A., Baše, J., Chum, J., Czanik,  
725 C., Ionescu, C., Neagoe, C. and Pásztor, M.: Central and Eastern European Infrasound Network:  
726 contribution to infrasound monitoring, *Geophysical Journal International*, 230(1), 565-579,  
727 <https://doi.org/10.1093/gji/ggac066>, 2022.
- 728 Borzì, A.M., Minio, V., Cannavò, F., Cavallaro, A., D'Amico, S., Gauci, A., De Plaen, R., Lecocq,  
729 T., Nardone, G., Orasi, A., Picone, M., Cannata, A.: Monitoring extreme meteo-marine events in  
730 the Mediterranean area using the microseism (Medicane Apollo case study). *Scientific Reports*,  
731 12(1), <https://doi.org/10.1038/s41598-022-25395-9>, 2022.
- 732 Bosy, J., Kaplon, J., Rohm, W., Sierny, J. and Hadas, T.: Near real-time estimation of water vapour  
733 in the troposphere using ground GNSS and the meteorological data, *Annales Geophysicae*, 30,  
734 1379–1391, <https://doi.org/10.5194/angeo-30-1379-2012>, 2012.
- 735 Brachet, N., Brown, D., Le Bras, R., Cansi, Y., Mialle, P., Coyne, J.: Monitoring the Earth's  
736 Atmosphere with the Global IMS Infrasound Network, in: *Infrasound Monitoring for Atmospheric*  
737 *Studies*, edited by: Le Pichon, A., Blanc, E., Hauchecorne, A. , Springer, Dordrecht,  
738 [https://doi.org/10.1007/978-1-4020-9508-5\\_3](https://doi.org/10.1007/978-1-4020-9508-5_3), 2010.
- 739 Bromirski, P.D. and Duennebieer, F.K.: The near-coastal microseism spectrum: Spatial and  
740 temporal wave climate relationships. *Journal of Geophysical Research: Solid Earth*, 107(B8), ESE  
741 5-1-ESE 5-20, <https://doi.org/10.1029/2001JB000265>, 2002.
- 742 Bruyninx, C., Habrich, H., Söhne, W., Kenyeres, A., Stangl, G. and Völksen, C.: Enhancement of  
743 the EUREF permanent network services and products, in: *Proceedings of the International*

744 Association of Geodesy, *Symposium on Geodesy for Planet Earth, Buenos Aires, Argentina, 31*  
745 *August-4 September 2009, 27-34, 2012.*

746 Burtin, A., Hovius, N. and Turowski, J.M.: Seismic monitoring of torrential and fluvial processes.  
747 *Earth Surface Dynamics*, 4(2), 285-307, <https://doi.org/10.5194/esurf-4-285-2016>, 2016.

748 Butler, R. and Aucan, J.: Multisensor, microseismic observations of a hurricane transit near the  
749 ALOHA cabled observatory. *Journal of Geophysical Research: Solid Earth*, 123(4), 3027-3046,  
750 2018.

751 Campus, P. and Christie, D.R.: Worldwide observations of infrasonic waves, in: Infrasonic  
752 monitoring for atmospheric studies, edited by: Le Pichon, A., Blanc, E., Hauchecorne, A.,  
753 Springer, Dordrecht, Netherlands, 185-234, [https://doi.org/10.1007/978-1-4020-9508-5\\_6](https://doi.org/10.1007/978-1-4020-9508-5_6), 2009.

754 Cansi, Y. and Pichon, A.L.: Infrasonic event detection using the progressive multi-channel  
755 correlation algorithm, in: *Handbook of signal processing in acoustics.*, edited by: Havelock, D.,  
756 Kuwano, S., Vorländer, M., Springer, New York, 1425-1435, [https://doi.org/10.1007/978-0-387-30441-0\\_77](https://doi.org/10.1007/978-0-387-30441-0_77), 2008.

758 Coates, A. and Ng, A.Y.: Learning feature representations with k-means. In *Neural Networks:*  
759 *Tricks of the Trade: Second Edition (561-580).* Berlin, Heidelberg: Springer Berlin Heidelberg,  
760 2012.

761 Coviello, V., Palo, M., Adirosi, E. and Picozzi, M.: Seismic signature of an extreme hydro-  
762 meteorological event in Italy, *Natural Hazards*, 1(1), 17, [https://doi.org/10.1038/s44304-024-](https://doi.org/10.1038/s44304-024-00018-7)  
763 [00018-7](https://doi.org/10.1038/s44304-024-00018-7), 2024.

764 Diaz, J., Ruiz, M., Udina, M., Polls, F., Martí, D., Bech, J.: Monitoring storm evolution using a  
765 high-density seismic network, *Scientific Reports*, 13(1), [https://doi.org/10.1038/s41598-023-](https://doi.org/10.1038/s41598-023-28902-8)  
766 [28902-8](https://doi.org/10.1038/s41598-023-28902-8), 2023.

767 Díaz, J., Ruiz, M., Sánchez-Pastor, P.S. and Romero, P.: Urban seismology: On the origin of earth  
768 vibrations within a city. *Scientific reports*, 7(1), 15296, 2017.

769 Dimitriu, R.G., Stanciu, I.M., Barbu M.-B., Dobrev, N., Dumitru, P.: First results on the western  
770 Black Sea coast geodynamics resulted from GeoPontica permanent GNSS stations network data  
771 processing, in: Proceedings of the 17th International Multidisciplinary Scientific GeoConference  
772 SGEM, Albena, Bulgaria August 2017, 17(11), 149-157, 2017.

773 Dullaart, J.C., Muis, S., Bloemendaal, N. and Aerts, J.C.: Advancing global storm surge modelling  
774 using the new ERA5 climate reanalysis. *Climate Dynamics*, 54(1), 1007-1021, 2020.

775 Ebeling, C.W.: Inferring Ocean Storm Characteristics from Ambient Seismic Noise. A Historical  
776 Perspective, *Advances in Geophysics*, 53, 1-33. [https://doi.org/10.1016/B978-0-12-380938-](https://doi.org/10.1016/B978-0-12-380938-4.00001-X)  
777 [4.00001-X](https://doi.org/10.1016/B978-0-12-380938-4.00001-X), 2012.

778 Faranda, D., Messori, G., Coppola, E., Alberti, T., Vrac, M., Pons, F., Yiou, P., Saint Lu, M., Hisi,  
779 A. N. S., Brockmann, P., Dafis, S., Mengaldo, G., and Vautard, R.: ClimaMeter: contextualizing  
780 extreme weather in a changing climate, *Weather Climate Dynamics*, 5, 959-983,  
781 <https://doi.org/10.5194/wcd-5-959-2024>, 2024.

782 Floroiu, I., Anghel, A., Petrescu, L. and Datcu, M.: Clustering and Feature-Based Similarity  
783 Retrieval of Infrasound Events during Two Storms in Constanța, Romania, *International  
784 Conference on Machine Intelligence for GeoAnalytics and Remote Sensing (MIGARS)*, Bucharest,  
785 Romania, 2025, 1-4, <https://doi.org/10.1109/MIGARS67156.2025.11231952>, 2025.

786 Francoeur, J.W., Matoza, R.S., Ortiz, H.D. and De Negri, R.: Identification of transient seismo-  
787 acoustic signals from crashing ocean waves: template matching and location of discrete surf  
788 events. *Geophysical Journal International*, 243(2), ggaf317, 2025.

789 Garcés, M.A.: On infrasound standards, part 1 time, frequency, and energy scaling. *InfraMatics*,  
790 2(2),13–35, <https://doi.org/10.4236/inframatics.2013.22002>, 2013.

791 Gastmeier, W.J. and Howe, B.: Recent studies of infrasound from industrial sources. *Canadian  
792 Acoustics*, 36(3), 58-59, 2008.

793 Grafkina, M.V., Nyunin, B.N. and Sviridova, E.Y: Environmental monitoring and simulation of  
794 infrasound generating mechanism of traffic flow. *Journal of Ecological Engineering*, 20(7),  
795 2019.

796 Grevemeyer, I., Herber, R. and Essen, H.H.: Microseismological evidence for a changing wave  
797 climate in the northeast Atlantic Ocean. *Nature*, 408(6810), 349-352,  
798 <https://doi.org/10.1038/35042558>, 2000.

799 Groos, J.C. and Ritter, J.R.R.: Time domain classification and quantification of seismic noise in  
800 an urban environment. *Geophysical Journal International*, 179(2), pp.1213-1231, 2009.

801 Gualtieri, L., Camargo, S.J., Pascale, S., Pons, F.M.E., & Ekström, G.: The persistent signature of  
802 tropical cyclones in ambient seismic noise, *Earth and Planetary Science Letters*, 484, 287-294.  
803 <https://doi.org/10.1016/j.epsl.2017.12.026>, 2018.

804 Guerova, G., Jones, J., Douša, J., Dick, G., de Haan, S., Pottiaux, E., Bock, O., Pacione, R.,  
805 Elgered, G., Vedel, H. and Bender, M.: Review of the state of the art and future prospects of the  
806 ground-based GNSS meteorology in Europe, *Atmospheric Measurement Techniques*, 9(11),  
807 5385–5406, <https://doi.org/10.5194/amt-9-5385-2016>, 2016.

808 Herring, T., King, R., Floyd, M., McClusky, S.: GAMIT Reference Manual GPS Analysis at MIT  
809 Release 10.7. GAMIT/GLOBK, 2020.

810 Hersbach, H., Bell, B., Berrisford, P., Hirahara, S., Horányi, A., Muñoz-Sabater, J., Nicolas, J.,  
811 Peubey, C., Radu, R., Schepers, D. and Simmons, A.: The ERA5 global reanalysis, *Quarterly  
812 Journal of the Royal Meteorological Society*, 146(730), 1999-2049, 2020.

813 Hersbach, H., Bell, B., Berrisford, P., Biavati, G., Horányi, A., Muñoz Sabater, J., Nicolas, J.,  
814 Peubey, C., Radu, R., Rozum, I., Schepers, D., Simmons, A., Soci, C., Dee, D., Thépaut, J.-N.:  
815 ERA5 hourly data on single levels from 1940 to present. Copernicus Climate Change Service  
816 (C3S) Climate Data Store (CDS), <https://doi.org/10.24381/cds.adbb2d47>, 2023.

817 Holmlund, K., Grandell, J., Schmetz, J., Stuhlmann, R., Bojkov, B., Munro, R., Lekouara, M.,  
818 Coppens, D., Viticchie, B., August, T. and Theodore, B.: Meteosat Third Generation (MTG):  
819 Continuation and innovation of observations from geostationary orbit, *Bulletin of the American*  
820 *Meteorological Society*, 102(5), E990-E1015, <https://doi.org/10.1175/BAMS-D-19-0304.1>, 2021.

821 Hua, J., Wu, M., Mulholland, J.P., Neelin, J.D., Tsai, V.C. and Trugman, D.T.: High-resolution  
822 precipitation monitoring with a dense seismic nodal array. *Scientific Reports*, 13(1), 11450,  
823 <https://doi.org/10.1038/s41598-023-38008-w>, 2023.

824 Hupe, P., Ceranna, L., Pilger, C., de Carlo, M., Le Pichon, A., Kaifler, B. and Rapp, M.: Assessing  
825 middle atmosphere weather models using infrasound detections from microbaroms. *Geophysical*  
826 *Journal International*, 216(3), 1761-1767, <https://doi.org/10.1093/gji/ggy520>, 2019.

827 Hupe, P., Ceranna, L., Le Pichon, A., Matoza, R.S. and Mialle, P.: International Monitoring  
828 System infrasound data products for atmospheric studies and civilian applications. *Earth System*  
829 *Science Data Discussions*, 14, 4201–4230, <https://doi.org/10.5194/essd-14-4201-2022>, 2022.

830 Iliescu, A. I., Rus, T., Danciu, V., Moldoveanu, C., & Ilie, A.: Current situation of GNSS networks  
831 in Romania, *Bulletin of University of Agricultural Sciences and Veterinary Medicine Cluj-Napoca.*  
832 *Horticulture*, 76(2), 2019.

833 Jakobsen, J.: Infrasound emission from wind turbines. *Journal of low frequency noise, vibration*  
834 *and active control*, 24(3), 145-155, 2005.

835 Jiao, D., Xu, N., Yang, F. and Xu, K.: Evaluation of spatial-temporal variation performance of  
836 ERA5 precipitation data in China. *Scientific Reports*, 11(1), 17956, 2021.

837 Johnston, G., Riddell, A. and Hausler, G.: The international GNSS service, in: Springer handbook  
838 of global navigation satellite systems, edited by: Teunissen, P.J. and Montenbruck, O., Springer,  
839 Cham, Switzerland, 967-982, [https://doi.org/10.1007/978-3-319-42928-1\\_33](https://doi.org/10.1007/978-3-319-42928-1_33), 2017.

840 Jones, J., Guerova, G., Douša, J., Dick, G., de Haan, S., Pottiaux, E., Bock, O., Pacione, R. and  
841 Van Malderen, R.: Advanced GNSS tropospheric products for monitoring severe weather events  
842 and climate, COST Action ES1206 Final Action Dissemination Report, 563, 2020.

843 Karabatić, A., Weber, R. and Haiden, T.: Near real-time estimation of tropospheric water vapour  
844 content from ground based GNSS data and its potential contribution to weather now-casting in  
845 Austria, *Advances in Space Research*, 47(10), 1691–1703,  
846 <https://doi.org/10.1016/j.asr.2010.10.028>, 2011.

847 Kober, K. and Tafferer, A.: Tracking and nowcasting of convective cells using remote sensing  
848 data from radar and satellite, *Meteorologische Zeitschrift*, 1(18), 75-84,  
849 <https://doi.org/10.1127/0941-2948/2009/359>, 2009.

850 Koper, K.D. & Burlacu, R.: The fine structure of double-frequency microseisms recorded by  
851 seismometers in North America. *Journal of Geophysical Research: Solid Earth*, 120(3), 1677-  
852 1691. <https://doi.org/10.1002/2014JB011820>, 2015.

853 Landès, M., Ceranna, L., Le Pichon, A. and Matoza, R.S.: Localization of microbarom sources  
854 using the IMS infrasound network. *Journal of Geophysical Research: Atmospheres*, 117(D6),  
855 <https://doi.org/10.1029/2011JD016684>, 2012.

856 Landskron, D., Böhm, J.: VMF3/GPT3: refined discrete and empirical troposphere mapping  
857 functions, *Journal of Geodesy*, 92, 349–360, <https://doi.org/10.1007/s00190-017-1066-2>, 2018.

858 Li, L., Boué, P., Retailleau, L., & Campillo, M.: Spatiotemporal Correlation Analysis of Noise-  
859 Derived Seismic Body Waves With Ocean Wave Climate and Microseism Sources, *Geochemistry,*  
860 *Geophysics, Geosystems*, 21(9), <https://doi.org/10.1029/2020GC009112>, 2020.

861 Listowski, C., Forestier, E., Dafis, S., Farges, T., De Carlo, M., Grimaldi, F., Le Pichon, A.,  
862 Vergoz, J., Heinrich, P. and Claud, C.: Remote monitoring of Mediterranean hurricanes using  
863 infrasound, *Remote Sensing*, 14(23), 6162, <https://doi.org/10.3390/rs14236162>, 2022.

864 MacQueen, J.: Some methods for classification and analysis of multivariate observations, in:  
865 Proceedings of the Fifth Berkeley Symposium on Mathematical Statistics and Probability,  
866 Berkeley, California, January 1967, 5, 281-298, 1967.

867 Marut, G., Hadas, T., Kaplon, J., Trzcina, E. and Rohm, W.: Monitoring the water vapor content  
868 at high spatio-temporal resolution using a network of low-cost multi-GNSS receivers, *IEEE*  
869 *Transactions on Geoscience and Remote Sensing*, 60, 1-14,  
870 <https://doi.org/10.1109/TGRS.2022.3226631>, 2022.

871 Pásztor, M., Czanik, C. and Bondár, I.: A single array approach for infrasound signal  
872 discrimination from quarry blasts via machine learning, *Remote Sensing*, 15(6), 1657,  
873 <https://doi.org/10.3390/rs15061657>, 2023.

874 Le Pichon, A., Matoza, R., Brachet, N. and Cansi, Y.: Recent enhancements of the PMCC  
875 infrasound signal detector. *Inframatrics*, 26, 5-8, 2010.

876 Price, I., Sanchez-Gonzalez, A., Alet, F., Andersson, T.R., El-Kadi, A., Masters, D., Ewalds, T.,  
877 Stott, J., Mohamed, S., Battaglia, P. and Lam, R.: Probabilistic weather forecasting with machine  
878 learning. *Nature*, 637(8044), 84-90, 2025

- 879 Priego, E., Jones, J., Porres, M.J. and Seco, A.: Monitoring water vapour with GNSS during a  
880 heavy rainfall event in the Spanish Mediterranean area, *Geomatics, Natural Hazards and Risk*,  
881 8(2), 282–294, <https://doi.org/10.1080/19475705.2016.1201150>, 2017.
- 882 Retailleau, L. & Gualtieri, L.: Multi-phase seismic source imprint of tropical cyclones, *Nature*  
883 *Communications*, 12(1), <https://doi.org/10.1038/s41467-021-22231-y>, 2021.
- 884 Rindraharisaona, E.J., Réchou, A., Fontaine, F.R., Barruol, G., Stamenoff, P., Boudevillain, B.,  
885 Rigaud-Louise, F. and Delcher, E.: Seismic signature of rain and wind inferred from seismic data,  
886 *Earth and Space Science*, 9(10), p.e2022EA002328, 2022.
- 887 Šindelářová, J., Chum, J., Skripnikova, K., and Base, J.: Atmospheric infrasound observed during  
888 intense convective storms on 9–10 July 2011, *Journal of Atmospheric and Solar-Terrestrial*  
889 *Physics*, 122, 66–74, <https://doi.org/10.1016/j.jastp.2014.10.014>, 2015.
- 890 Šindelářová, T., De Carlo, M., Czanik, C., Ghica, D., Kozubek, M., Podolská, K., Baše, J., Chum,  
891 J., and Mitterbauer, U.: Infrasound signature of the post-tropical storm Ophelia at the Central and  
892 Eastern European Infrasound Network, *Journal of Atmospheric and Solar-Terrestrial Physics*, 217,  
893 105603, <https://doi.org/10.1016/j.jastp.2021.105603>, 2021.
- 894 Smirnov, A., De Carlo, M., Le Pichon, A., Shapiro, N.M. and Kulichkov, S.: Characterizing the  
895 oceanic ambient noise as recorded by the dense seismo-acoustic Kazakh network. *Solid Earth*,  
896 12(2), 503-520, 2021.
- 897 Soci, C., Hersbach, H., Simmons, A., Poli, P., Bell, B., Berrisford, P., Horányi, A., Muñoz-Sabater,  
898 J., Nicolas, J., Radu, R. and Schepers: The ERA5 global reanalysis from 1940 to 2022. *Quarterly*  
899 *Journal of the Royal Meteorological Society*, 150(764), 4014-4048, 2024.
- 900 Sokol, Z., Szturc, J., Orellana-Alvear, J., Popova, J., Jurczyk, A. and Célleri, R.: The role of  
901 weather radar in rainfall estimation and its application in meteorological and hydrological  
902 modelling—A review, *Remote Sensing*, 13(3), 351, 2021.
- 903 Stopa, J.E., Cheung, K.F., Garcés, M.A. and Badger, N.: Atmospheric infrasound from nonlinear  
904 wave interactions during Hurricanes Felicia and Neki of 2009, *Journal of Geophysical Research:*  
905 *Oceans*, 117(C12), <https://doi.org/10.1029/2012JC008257>, 2012
- 906 Stott, P.: How climate change affects extreme weather events. *Science*, 352(6293), 1517-1518,  
907 <https://doi.org/10.1126/science.aaf7271>, 2016.
- 908 Tanimoto, T. & Anderson, A.: Seismic noise between 0.003 Hz and 1.0 Hz and its classification,  
909 *Progress in Earth and Planetary Science*, 10(1), <https://doi.org/10.1186/s40645-023-00587-7>,  
910 2023.
- 911 Taweessintananon, K., Landrø, M., Potter, J.R., Johansen, S.E., Rørstadbotnen, R.A., Bouffaut, L.,  
912 Kriesell, H.J., Brenne, J.K., Haukanes, A., Schjelderup, O. and Storvik, F.: Distributed acoustic

913 sensing of ocean-bottom seismo-acoustics and distant storms: A case study from Svalbard,  
914 Norway. *Geophysics*, 88(3), B135-B150, 2023.

915 Tiberia, A., Mascitelli, A., D’adderio, L.P., Federico, S., Marisaldi, M., Porcù, F., Realini, E.,  
916 Gatti, A., Ursi, A., Fuschino, F. and Tavani, M.: Time evolution of storms producing terrestrial  
917 gamma-ray flashes using ERA5 reanalysis data, GPS, lightning and geostationary satellite  
918 observations. *Remote Sensing*, 13(4), 784, 2021.

919 Vaquero-Martínez, J. and Antón, M.: Review on the role of GNSS meteorology in monitoring  
920 water vapor for atmospheric physics, *Remote Sensing*, 13(12), 2287,  
921 <https://doi.org/10.3390/rs13122287>, 2021.

922 Viticchie, B., Lekouara, M., Hungershöfer, K., Joro, S., Grandell, J., Maufrais, A., Marquez, M.J.,  
923 Munro, R.: Algorithm Theoretical Basis Document (ATBD) for L2 processing of the MTG  
924 Lightning Imager data, Rapp. Tech. EUMESTAT, 6, 2020.

925 Waxler, R., Frazier, W. G., Talmadge, C. L., Liang, B., Hetzer, C., Buchanan, H., and Audette, W.  
926 E.: Analysis of infrasound array data from tornadic storms in the southeastern United States,  
927 *Journal of the Acoustical Society of America*, 156, 1903–1919,  
928 <https://doi.org/10.1121/10.0028815>, 2024.

929 Wessel, P., Luis, J.F., Uieda, L.A., Scharroo, R., Wobbe, F., Smith, W.H. and Tian, D.: The generic  
930 mapping tools version 6, *Geochemistry, Geophysics, Geosystems*, 20(11), 5556-5564,  
931 <https://doi.org/10.1029/2019GC008515>, 2019.

932 Wilgan, K., Rohm, W. and Bosy, J.: Multi-observation meteorological and GNSS data comparison  
933 with numerical weather prediction model, *Atmospheric Research*, 156, 29–42,  
934 <https://doi.org/10.1016/j.atmosres.2014.12.011>, 2015.

935 Wu, G., Qin, S., Mao, Y., Ma, Z. and Shi, C.: Validation of precipitation events in ERA5 to gauge  
936 observations during warm seasons over eastern China. *Journal of Hydrometeorology*, 23(5), 807-  
937 822, 2022.  
938